Analysis and Experimentation of a Novel Modulation Technique for a Dual-Output WPT Inverter

Manuele Bertoluzzo, Giuseppe Buja, *Life Fellow, IEEE*, and Hemant Kumar Dashora, *Member, IEEE*

***Abstract*—Dynamic wireless power transfer systems require to supply many transmitting coils deployed under the road surface and arranged along the so-called track. This layout entails the use of a large number of inverters or of devices that switch the power to the proper coils. This article presents a technique that uses a single three-phase inverter to supply two coils with voltages having different and independently adjustable amplitudes of their first harmonic component. Differently from the well-known phase shift technique, the amplitude and the phase of the voltages are not correlated. Moreover, the presented technique has the ability of inherently reducing the phase difference between the two output currents when the supplied loads are partially reactive. This feature enhances the power transfer capability of the inverter when both the track coils are coupled with the same pickup. After presenting this technique, this article analyzes the functioning of the dual-output inverter in different load conditions recognizing the boundaries of four different modes of operation. For each of them the analytical expression of the amplitude and phase of the generated voltages are given. The theoretical findings are validated by experiments performed on a prototypal setup that implements the presented modulation technique.**

***Index Terms*—Inductive power transmission, phase control, voltage source inverters, wireless power transfer.**

I. Introduction

WIRELESS power transfer (WPT) based on magnetic induction is the subject of advanced studies that aim at transferring power onboard electric vehicles running on suitable tracks [1], [2], [3]. Implementation of tracks requires to design carefully the transmitting coils [4], their reciprocal placement [5], and their supply system. The latter one could include a large number of inverters and, hence, it is mandatory to optimize its architecture. Some proposals have been presented to minimize the complexity and the cost of the supply infrastructure by using only one inverter and relying on the interaction between the transmitting coils to transfer energy to a pickup coupled to any of them [6], [7]. With this arrangement, however, it is not possible to control independently the coils as all of them are always energized. Other approaches are based on switches that forward the power supplied by the inverter only to the track coils that must be energized; the switches are implemented by static devices [8], [9] or by additional inductors whose cores are on purpose saturated to control the power transfer [10]; another solution exploits the inherent variation of the impedance of the track coil coupled to the pickup to forward the supply power to it [11]. These approaches do not allow to control independently the power supplied to the energized coils and this could be a limiting factor if, depending on the distance between two subsequent track coils and on their dimension, the pickup is temporary coupled simultaneously with two of them [5]. In this case, both the track coils contribute to the power transfer, which is maximum when the currents flowing in the coils are in phase so as to sum the magnetic fluxes linked with the pickup. The same requirement is found also in [12], where the currents in the two subcoils of a track DD coil are controlled separately. Besides the phase relation between the currents, it is also important to control independently their amplitude to maximize the WPT system (WPTS) efficiency; Huh and Ahn [13] and Kim and Ahn [14] used separate inverters to supply the track coils, increasing the complexity of the infrastructure, and requiring to exchange some data between the inverters control stages [13] to synchronize the phases of the output currents.

A solution to reduce the cost and the complexity of the infrastructure is proposed in [15], where a PWM technique for a three-legs inverter with two outputs is presented. It allows to save two power switches with respect to the conventional solution of using two two-legs inverters. The same scheme is generalized in [16] for the supply of multiple track coils.

Considering that the surface vehicle standard J2954 issued by SAE [17] fixes to 85 kHz the nominal supply frequency f_s of the wireless charging stations, the PWM technique proposed in [15] is not viable to control the amplitude of the high frequency inverter (HFI) output voltage. Instead, in WPTSs, the phase shift technique (PST) is commonly used [18], [19], even if some authors propose to supply the transmitting coils with a square-wave voltage [16].

An original technique for the command of the HFI power switches has been presented in [20]. This technique is derived

Manuscript received 29 July 2022; revised 18 October 2022 and 7 November 2022; accepted 29 November 2022. *(Corresponding author: Manuele Bertoluzzo.)*

Manuele Bertoluzzo and Giuseppe Buja are with the Department of Industrial Engineering, University of Padova, 35131 Padova, Italy (e-mail: manuele.bertoluzzo@unipd.it; giuseppe.buja@unipd.it).

Hemant Kumar Dashora is with the KPIT Technologies Ltd., Pune 411057, India (e-mail: hemant.dashora@kpit.com).

Color versions of one or more figures in this article are available at https://doi.org/10.1109/TIE.2022.3227298.

Digital Object Identifier 10.1109/TIE.2022.3227298

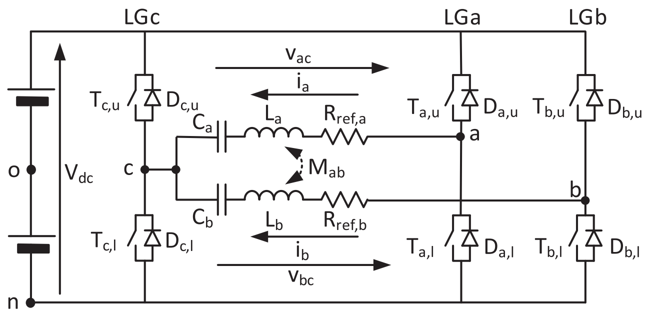

Fig. 1. Circuital scheme of the single output HFI (legs LGa and LGc) and of the dual output HFI (all the three legs).

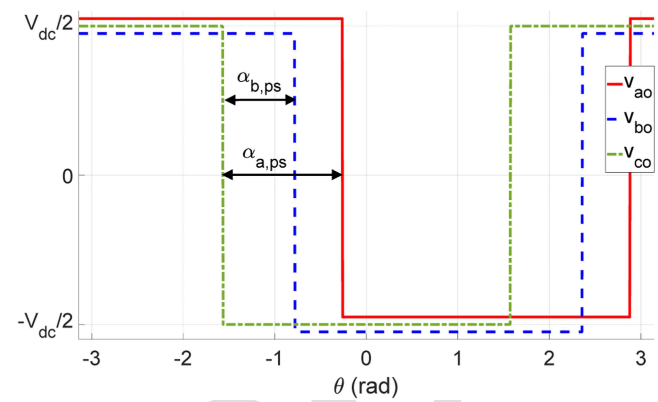

Fig. 2. Voltages v_{co}, v_{bo}, and v_{co} generated by PST.

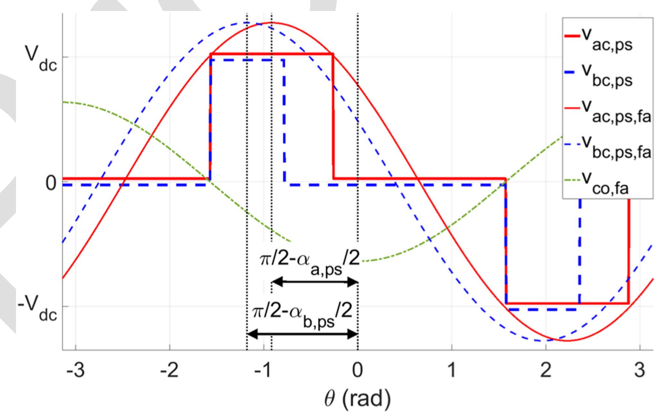

Fig. 3. Voltages $v_{ac,ps}$, $v_{bc,ps}$ and their first harmonic components generated by PST.

from the PST but, differently from it, allows to supply simultaneously two coils with two voltages whose amplitudes are adjusted independently while maintaining their phase relation. Moreover, when the loads seen at the HFI outputs are partially reactive, this technique exhibits the inherent ability of adjusting the phases of the output voltages in order to reduce the phase difference between the two output currents. With respect to [20], this article gives a much deeper mathematical analysis of the functioning and performance of the presented technique and, to this aim, uses the phasor notation to describe the generated voltages. The findings of the theoretical analysis are validated by the results of experimental tests.

The rest of this article is organized as follows. Section II reviews the functioning and the limitations of the PST and introduces the phasor representation used in the subsequent sections. Section III describes the proposed technique, and analyzes its operation with resistive loads. Section IV considers the effects of a partially reactive load on the amplitude and the phase of the output voltages. Section V demonstrates and quantifies the ability of the proposed technique to reduce the phase difference between the output currents. Section VI reports the results of the tests performed on a prototypal WPTS. Finally, Section VII concludes this article.

II. Phase Shift Technique

A. Conventional Phase Shift Technique

A single track coil can be supplied using an HFI formed by the two legs LGa and LGc sketched in Fig. 1. According to the PST, the power switches are commanded with square-wave gate signals to generate the two voltages v_{co} and v_{ao}. They can be expressed as

$$v_{co} = \text{square}\left(\omega_s t + \frac{\pi}{2}\right) \tag{1}$$

$$v_{ao} = \text{square}\left(\omega_s t + \frac{\pi}{2} - \alpha_{a,ps}\right) \tag{2}$$

where square(θ) is a square wave function having the falling edge at $\theta = 0$, $\omega_s = 2\pi \cdot f_s$ is the supply angular frequency and $\alpha_{a,ps}$ is the phase shift between the gate signals of the two legs. The voltages v_{co} and v_{ao} are plotted in Fig. 2 with the red solid line and the green dash-dotted line, respectively. In drawing the figure and in the subsequent discussion, the effects of the dead-times and of the finite commutation times are neglected. In this and in the following figures, a small offset is added to the square wave voltages in order to make it easier to distinguish them from each other.

The actual waveform of the output voltage v_{ac}, equal to

$$v_{ac,ps} = v_{ao} - v_{co} \tag{3}$$

is imposed by the phase shift $\alpha_{a,ps}$, which lies in the interval (0,π). When $\alpha_{a,ps} = 0$, v_{ao} is in phase with v_{co} and the output voltage $v_{ac,ps}$ is nullified; when $\alpha_{a,ps} = \pi$, v_{ao}, and v_{co} are in phase opposition and $v_{ac,ps}$ has a square waveform with twice the amplitude of v_{ao} and v_{co}. In general, $v_{ac,ps}$ has the three-level waveform shown by the red solid line in Fig. 3. In each semi period the length of the phase interval with nonzero voltage is equal to $\alpha_{a,ps}$.

Usually the coils of a WPTS are connected to suitable compensation networks made of reactive elements [21]. In Fig. 1, the compensation network of the coil a is formed by the series capacitor C_a that resonates with the coil inductance L_a. The impedance $R_{ref,a}$ accounts for the coil parasitic resistance and the equivalent load of the pickup side of the WPTS reflected to the transmitting side. If the series resonance is enforced at the pickup side, $R_{ref,a}$ results purely resistive.

The series resonant compensation introduces a minimum of the reactance seen at the inverter output in correspondence with the supply frequency. Consequently, the inverter output current is nearly sinusoidal despite the quasi-square waveform of the output voltage. From this condition it derives that the power transferred to the pickup is mainly dependent on the first harmonic component of the supply voltage and is only marginally affected by its higher order harmonics. For this reason, it is a common practice in the analysis of the WPTSs to consider only the first harmonic component of the output voltage rather than its actual waveform. The first harmonic component $v_{ac,ps,fa}$ of $v_{ac,ps}$ is expressed by

$$v_{ac,ps,fa} = V_{ac,ps} \cos(\omega_s t + \theta_{vac,ps}) \tag{4}$$

and is plotted in Fig. 3 using the thin red solid line.

Its amplitude $V_{ac,ps}$ is

$$V_{ac,ps} = V_{dc}\frac{4}{\pi} \sin\left(\frac{\alpha_{a,ps}}{2}\right) \triangleq V_M \sin\left(\frac{\alpha_{a,ps}}{2}\right) \tag{5}$$

where V_M is the maximum amplitude achievable by first harmonic component of the inverter output voltage with the given dc side voltage V_{dc}. The initial phase $\theta_{vac,ps}$ is measured with respect to the central point of the negative half period of v_{co} and results

$$\theta_{vac,ps} = \frac{\pi}{2} - \frac{\alpha_{a,ps}}{2}. \tag{6}$$

The simultaneous supply of two or more track coils can be performed using independent HFIs, however, it is possible to reduce the cost and the complexity of the WPTS by arranging the coils into pairs and supplying each pair using a three-legs HFI, as shown in Fig. 1. In this way, the power switches of the legs LGa and LGb are flown by the currents i_a and i_b, while LGc sustains the current i_c, equal to the sum of i_a and i_b.

Applying the PST with the phase shift angle $\theta_{b,ps}$ to the gate command of LGb and LGc, $v_{bc,ps}$ is obtained at the second output of the HFI according to

$$v_{bc,ps} = v_{bo} - v_{co} . \tag{7}$$

The amplitude $V_{bc,ps}$ of its first harmonic component can be adjusted independently from $V_{ac,ps}$, but, following from (6), if the phase shift angle $\alpha_{b,ps}$ differs from $\alpha_{a,ps}$, the phase $\theta_{vbc,ps}$ results different from $\theta_{vac,ps}$, as shown in Fig. 3 using the thin blue dashed line.

In the hypothesis that the reflected load is substantially resistive for both the track coils, as it usually happens when series compensation is used in the pickup, a phase displacement between the supply voltages entails an about equal phase displacement between i_a and i_b, thus impairing the power transfer capability of the WPTS when the two track coils supply the same pickup.

B. Phasor Representation of the Generated Voltages

To represent with more effectiveness the differences between the PST and the proposed technique, the phasor notation is introduced. Given the phase reference used in (4) and (6), the real axis of the phasor diagram corresponds to the opposite of the phasor of the first harmonic components $v_{co,fa}$ of v_{co}, represented in Fig. 3 using the thin green dash-dotted line.

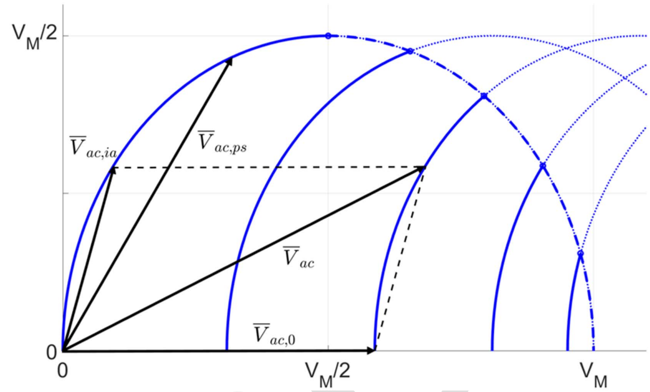

Fig. 4. Phasor representation of the output voltage.

The phasor of $v_{ac,ps,fa}$ is denoted as $\overline{V}_{ac,ps}$. Its components are derived from (5) and (6) with some manipulations that involve the use of the double-angle and the half-angle formulas

$$\begin{cases} v_{ac,ps,Re} = \frac{V_M}{2}(1-\cos(\alpha_{a,ps})) \\ v_{ac,ps,Im} = \frac{V_M}{2} \sin(\alpha_{a,ps}) \end{cases} . \tag{8}$$

By expressing $v^2_{ac,ps,Im}$ as a function of $v^2_{ac,ps,Re}$ and $v_{ac,ps,Re}$, the relation (9) is obtained

$$v^2_{ac,ps,Im} + \left(v_{ac,ps,Re} - \frac{V_M}{2}\right)^2 = \left(\frac{V_M}{2}\right)^2. \tag{9}$$

Equations (8) and (9) reveal that while $\alpha_{a,ps}$ spans the interval $(0,\pi)$, the tip of $\overline{V}_{ac,ps}$ moves from (0,0) to $(V_M,0)$ along the semi-circumference centered in $(V_M/2,0)$ and having radius equal to $V_M/2$, as shown in Fig. 4.

III. Partially Imposed Voltage Technique

The modulation technique presented in [20] is based on the hypothesis that the currents supplied by the dual-output HFI flow for the full supply period, as it usually happens when the WPTS operates in resonance. This technique allows to adjust independently the amplitudes V_{ac} and V_{bc} while maintaining the phase relation

$$\theta_{vac} - \theta_{vbc} = 0. \tag{10}$$

In the same way as PST, the power switches of LGc are commanded with a 50% duty cycle, so that the voltage v_{co}, represented by the thick green dash-dotted line in the upper half of Fig. 5, is imposed during the full supply period. Differently from PST, there are not negligible intervals of the supply period during which neither the upper nor the lower switches of LGa and/or LGb are closed. In these intervals, the actual voltages v_{ao} and v_{bo} are not imposed by the switching commands but are dictated by the currents at the HFI outputs, which force the conduction of either the upper or the lower free-wheeling diodes. For this reason, the presented technique is designed as partially imposed voltage technique (PIVT).

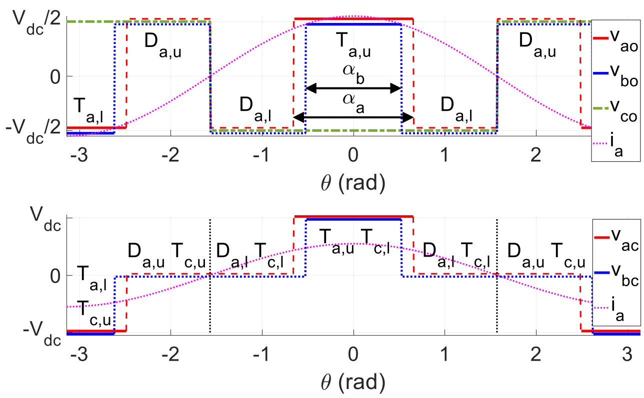

Fig. 5. Voltage waveforms generated by PIVT with $\theta_{ia} = \theta_{ib} = 0$.

More in details, as shown in the upper half of Fig. 5, the PIVT closes the upper switch $T_{a,u}$ of LGa only for an interval centered around 0 and spanning α_a radians, and the lower switch $T_{a,l}$ of the same leg for an equal interval centered around π. Consequently, the power switches of LGa are turned ON and OFF one time per supply period, like it happens in PST. While $T_{a,u}$ or $T_{a,l}$ are closed, the voltage v_{ao} is equal to V_{dc} or to $-V_{dc}$, respectively, as highlighted by the thick red solid line. When both the power switches are open, in agreement with the conventions of Fig. 1, at the positive zero crossing of current i_a, the upper freewheeling diode $D_{a,u}$ of LGa is forced to turn OFF while the lower freewheeling diode $D_{a,l}$ is forced to turn ON, driving v_{ao} to $-V_{dc}$. At the negative zero crossing of i_a, $D_{a,u}$ is forced to turn ON, $D_{a,l}$ is forced to turn OFF, and v_{ao} is driven to V_{dc}. When $T_{a,u}$ is turned ON and OFF, $D_{a,l}$ is forced to turn OFF and ON, respectively. The same happens with the pair $T_{a,l}$-$D_{a,u}$.

If i_a is in phase to $-v_{co,fa}$, as exemplified by the magenta dotted line of Fig. 5, the waveform of v_{ao} results as reported in the upper half of the figure, where the voltages due to the diode conduction are represented by the thin red dashed line. The output voltage $v_{ac} = v_{ao} - v_{co}$ is plotted in the lower half of Fig. 5, using the thick red solid line when the voltage is imposed by the power switches and the thin red dashed line when it is driven by the diodes. Obviously, PIVT is used also to command the power switches of LGb. If the current i_b is in phase to $-v_{co,fa}$, the voltages v_{bo} and v_{bc} have the waveforms plotted with the blue lines, the difference with respect to v_{ao} and v_{ac} being that the length of the power switches conduction intervals is α_b instead of α_a.

The waveforms of v_{ac} and v_{bc} are the same obtained with the PST but their phase is different as they are symmetric with respect to $\theta = 0$. Thanks to this symmetry, it results

$$\theta_{vac} = \theta_{vbc} = 0 \tag{11}$$

for any pair of α_a and α_b so that (10) is always verified. By (11), the two voltages result in phase to $-v_{co,fa}$ and, hence, they are in phase to i_a and i_b.

Equation (5) holds also for the amplitude of the first harmonic components of v_{ac} and v_{bc}. For v_{ac}, it is rewritten as

$$V_{ac,0} = V_M \sin\left(\frac{\alpha_a}{2}\right) \tag{12}$$

where the subscript "0" denotes that (12) refers to the condition of having i_a in phase to $v_{ac,fa}$. A similar relation holds also for $V_{bc,0}$ provided that α_b is used instead of α_a.

The components of $\overline{V}_{ac,0}$ are

$$\begin{cases} v_{ac,0,Re} = & V_M \ sin\left(\frac{\alpha_a}{2}\right) \\ v_{ac,0,Im} = & 0 \end{cases} \tag{13}$$

and while α_a varies in (0,π), the tip of the phasor $\overline{V}_{ac,0}$ moves from (0,0) to (V_M,0) along the real axis of Fig. 4.

The results of this section can be summarized by stating that if the loads seen at the HFI outputs are purely resistive, the currents i_a and i_b are in phase each to the other irrespectively from the relevant output voltages.

IV. Effect of Load Reactance

Generally speaking, if the track coils are coupled each other with the mutual inductance M_{ab} and with the pickup with the mutual inductances M_{ap} and M_{bp}, the expressions that link the supply voltages to the track coils currents are

$$\begin{cases} \overline{V}_{ac} = \left(\dot{Z}_a + \frac{\omega_s^2 M_{ap}^2}{\dot{Z}_p}\right)\bar{I}_a + \left(j\omega_s M_{ab} + \frac{\omega_s^2 M_{ap} M_{bp}}{\dot{Z}_p}\right)\bar{I}_b \\ \overline{V}_{bc} = \left(\dot{Z}_b + \frac{\omega_s^2 M_{bp}^2}{\dot{Z}_p}\right)\bar{I}_b + \left(j\omega_s M_{ab} + \frac{\omega_s^2 M_{ap} M_{bp}}{\dot{Z}_p}\right)\bar{I}_a \end{cases} \tag{14}$$

where $\dot{Z}_a$ and $\dot{Z}_b$ are the impedances of the assemblies made of the track coils and their compensation networks whilst $\dot{Z}_p$ is the impedance that accounts for the pickup, its compensation network and the load reflected at the input of the high frequency rectifier (HFR) that conditions the voltage induced across the pickup.

While the mutual inductance M_{ab} can be reduced by properly designing the coils [22] or by setting up a proper decoupling solution [23], the track coils interaction due to the coupling with the pickup cannot be avoided if both of them supply it at the same time. However, if the track coils and the pickup are series-compensated, the three impedances $\dot{Z}_a$, $\dot{Z}_b$, and $\dot{Z}_p$ are purely resistive and if $\overline{V}_{ac}$ and $\overline{V}_{ac}$ are in-phase, the same happens also for the currents.

The hypothesis of having purely resistive impedances $\dot{Z}_a$, $\dot{Z}_b$, and $\dot{Z}_p$ cannot be assured in practical application because of the tolerance on the components of the compensation networks, their variations with ageing, the dependence of the self-inductances and mutual inductance of the track coils and of the pickup to their relative positions.

Any of these causes originates a phase displacement between the currents i_a and i_b and the first harmonic components $v_{ac,fa}$ and $v_{bc,fa}$ of the relevant HFI output voltages. In the subsequent analysis it is supposed that the phase displacement can take any value even if, in a practical application, only the interval ($-\pi/2$,$\pi/2$) should be considered, otherwise the power would flow back from the load to the dc side of the HFI. In order to simplify the discussion, only the effect of a phase lag of i_a with respect to $-v_{co,fa}$ will be considered, with the awareness that the results can be easily adapted to the case of i_a leading $-v_{co,fa}$, and extended to the current i_b. Moreover, it is also supposed that $\alpha_a > 0$ whilst the generalization of the results to the case $\alpha_a = 0$ is reported in the next Section.

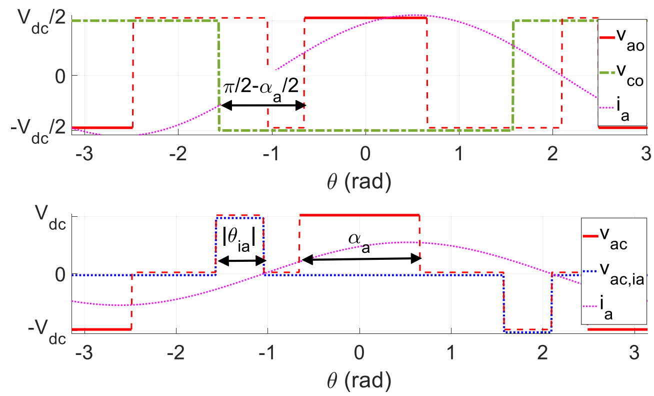

Fig. 6. Voltage waveforms generated by PIVT in mode A.

By analysis of Fig. 5, three modes of operation can be recognized: a) i_a changes its sign from negative to positive before $T_{a,u}$ is switched ON; b) i_a changes sign while $T_{a,u}$ is ON; c) i_a changes its sign after $T_{a,u}$ is switched OFF.

Each mode originates a different behavior and must be studied separately. In all the cases i_a is considered sinusoidal and is expressed as

$$i_a = I_a \cos(\omega_s t + \theta_{ia}). \tag{15}$$

A. $(\alpha_a/2 - \pi/2) < \theta_{ia} < 0$

This situation is exemplified in Fig. 6. By comparison with Fig. 5, it results that there are two more phase intervals where the HFI output voltage v_{ac} is different from zero. During the first interval, which begins at the falling edge of v_{co} and extends for a phase interval equal to $|\theta_{ia}|$, i_a maintains the conduction of $D_{a,u}$ so that v_{ac} results equal to V_{dc}. During the second interval, which has the same phase length and begins at the rising edge of v_{co}, the conducting diode is $D_{a,l}$ and v_{ac} is equal to -V_{dc}.

The voltage v_{ac} can be expressed as the sum of the output voltage plotted in Fig. 5 and relevant to the case of $\theta_{ia} = 0$, and of the voltage $v_{ac,ia}$, plotted with the blue dotted line in the lower half of Fig. 6, which includes only the two additional conduction intervals originated by the reactive component of i_a. The waveform of $v_{ac,ia}$ is similar to that of Fig. 3 and, hence, the parameters of its first harmonic components $v_{ac,ia,fa}$ are easily derived from (5) and (6) as

$$V_{ac,ia} = -V_M \sin\left(\frac{\theta_{ia}}{2}\right) \tag{16}$$

$$\theta_{vac,ia} = \frac{\pi}{2} + \frac{\theta_{ia}}{2} \tag{17}$$

where θ_{ia} is negative because, by hypothesis, $(\alpha_a/2 - \pi/2) < \theta_{ia} < 0$.

Equations (16) and (17) show that, differently from what happens with α_a, the angle θ_{ia} affects the phase of $v_{ac,ia,fa}$ besides its amplitude, and hence, it effects the phase of $v_{ac,fa}$.

The phasor of $v_{ac,fa}$ can be decomposed as in Fig. 4 in two contributes

$$\overline{V}_{ac} = \overline{V}_{ac,0} + \overline{V}_{ac,ia}. \tag{18}$$

The first of them is aligned with the real axis and has the components given by (13) while the components of $\overline{V}_{ac,ia}$, derived from (16) and (17) are

$$\begin{cases} v_{ac,ia,Re} = \frac{V_M}{2}\left(1 - \cos(\theta_{ia})\right) \\ v_{ac,ia,Im} = -\frac{V_M}{2} \sin(\theta_{ia}). \end{cases} \tag{19}$$

From the comparison of (19) with (8) and by remembering that θ_{ia} is negative it can be concluded that the tip of $\overline{V}_{ac,ia}$ moves on the same semicircumference as the tip of $\overline{V}_{ac,ps}$. In the limit condition of $\alpha_a = 0$ and in the hypothesis that also in this case i_a flows for the full supply period, the constraint $(\alpha_a/2 - \pi/2) < \theta_{ia} < 0$ states that θ_{ia} could span the interval $(-\pi/2, 0)$ and that, consequently, the tip of $\overline{V}_{ac}$, which in this limit condition is equal to $\overline{V}_{ac,ia}$, would move on the arc of the semicircumference beginning at $(V_M/2, V_M/2)$ and ending at (0,0). This is denoted as the maximum arc.

In realistic operating conditions α_a is bigger than zero and as it increases, θ_{ia} can span a reducing angular interval so that the tip of $\overline{V}_{ac,ia}$ moves on shorter and shorter sections of the maximum arc, beginning at the point

$$\begin{cases} v_{ac,ia,Re,\max} = \frac{V_M}{2}\left(1 - \sin\left(\frac{\alpha_a}{2}\right)\right) \\ v_{ac,ia,Im,\max} = \frac{V_M}{2} \cos\left(\frac{\alpha_a}{2}\right) \end{cases} \tag{20}$$

and ending at (0,0). Equation (20) is obtained from (19) by setting $\theta_{ia} = -\pi/2 + \alpha_a/2$.

From (18), (19), and (13), the components of the phasor $\overline{V}_{ac}$ result

$$\begin{cases} v_{ac,Re} = \frac{V_M}{2}\left[2\sin\left(\frac{\alpha_a}{2}\right) + 1 - \cos(\theta_{ia})\right] \\ v_{ac,Im} = -\frac{V_M}{2} \sin(\theta_{ia}) \end{cases} \tag{21}$$

from them, the amplitude and the phase of $\overline{V}_{ac}$ are readily derived as

$$V_{ac} = \frac{V_M}{2}\sqrt{\left[2\sin\left(\frac{\alpha_a}{2}\right) + 1 - \cos(\theta_{ia})\right]^2 + [\sin(\theta_{ia})]^2} \tag{22}$$

$$\theta_{vac,1} = atan\left[-\frac{\sin(\theta_{ia})}{2\sin\left(\frac{\alpha_a}{2}\right) + 1 - \cos(\theta_{ia})}\right]. \tag{23}$$

For a given value of α_a, V_{ac} results higher than $V_{ac,0}$ because of the contribute of $\overline{V}_{ac,ia}$, but in any case, V_{ac} never exceeds V_M, which is reached when $\alpha_a = \pi$ and $\overline{V}_{ac,ia}$ is null.

For any value of α_a in $(0,\pi)$, while θ_{ia} spans the interval $(\alpha_a/2 - \pi/2, 0)$, the tip of $\overline{V}_{ac}$ moves on an arc originating at

$$\begin{cases} v_{ac,Re,\max} = \frac{V_M}{2}\left(1 + \sin\left(\frac{\alpha_a}{2}\right)\right) \\ v_{ac,Im,\max} = \frac{V_M}{2} \cos\left(\frac{\alpha_a}{2}\right) \end{cases} \tag{24}$$

and ending at $(V_M \cdot \sin(\alpha_a/2), 0)$. The origins of these arcs lie on the quarter of circumference drawn with the blue dash-dotted line in Fig. 4. It is denoted as limit arc because, together the maximum arc, it bounds the semicircle where all the possible phasors $\overline{V}_{ac}$ fall.

Fig. 4 reports an example of the decomposition of $\overline{V}_{ac}$ according to (18) and all the possible positions of its tip for five different values of α_a. When $\alpha_a = 0$ the maximum arc on the left, expressed by (19), is obtained; as α_a increases the arcs

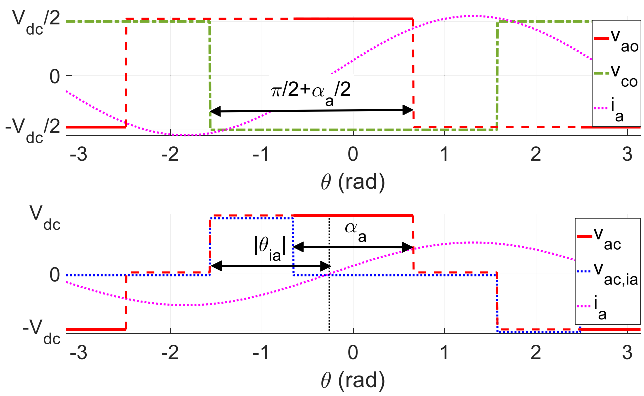

Fig. 7. Voltage waveforms generated by PIVT in mode B.

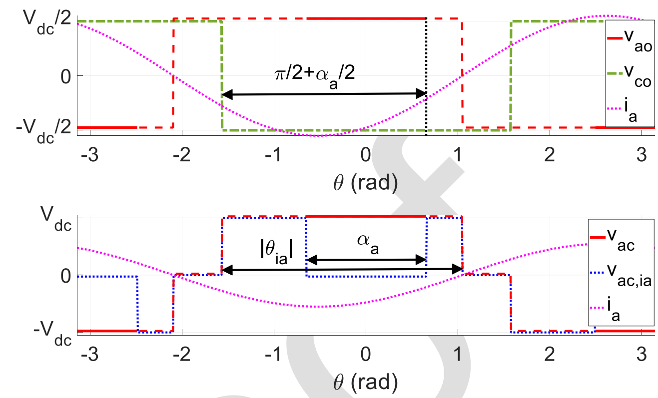

Fig. 8. Voltage waveforms generated by PIVT in mode C.

origins move to the right on the limit arc and the arcs length diminishes. Any two arcs intersect only outside the boundary semicircumference and, consequently, for any given phasor $\overline{V}_{ac}$ there is only one pair of α_a and θ_{ia} that realize it.

The analysis of the PIVT when i_a leads $-v_{co,fa}$ and $0 \leq \theta_{ia} \leq (\pi/2 - \alpha_a/2)$ is readily derived from the previous results considering that in this situation the conduction intervals of the diodes are on the right of the power switches conduction intervals instead that on the left. As a consequence, the phase of $\overline{V}_{ac,ia}$ is negative and the phasor diagram of Fig. 4 must be redrawn symmetrically with respect to the real axis.

B. $(-\alpha_a/2 - \pi/2) \leq \theta_{ia} \leq (\alpha_a/2 - \pi/2)$

This mode is exemplified in Fig. 7. By comparison with Fig. 6, it results that now the intervals of diode conduction extend up to the turning ON of the power switches. As a consequence, the output voltage v_{ac} results positive from $-\pi/2$ to α_a and negative from $\pi/2$ to $\pi+\alpha_a$ with a waveform that depends on α_a only, being the same that would have been obtained using the PST with $\alpha_{\mathrm{a,ps}} = \pi/2+\alpha_a/2$. The amplitude and the phase of $\mathrm{v}_{\mathrm{ac,fa}}$ are then expressed by (25) and (26), obtained from (5) and (6)

$$V_{ac} = V_M \sin\left(\frac{\pi}{4} + \frac{\alpha_a}{4}\right) \quad (25)$$

$$\theta_{vac} = \frac{\pi}{4} - \frac{\alpha_a}{4}. \quad (26)$$

The components of $\overline{V}_{ac}$ are worked out manipulating (25) and (26) obtaining expressions equal to (24), thus demonstrating that while α_a spans the interval $(0,\pi)$, the tip of $\overline{V}_{ac}$ lies on the limit arc.

As in the previous mode, if the current i_a leads $-v_{co,fa}$ and $(\pi/2 - \alpha_a/2) \leq \theta_{ia} \leq (\pi/2+\alpha_a/2)$, the findings are still valid provided that the diagram of Fig. 4 is redrawn symmetrically with respect to the real axis.

C. $-\pi \leq \theta_{ia} \leq (-\alpha_a/2 - \pi/2)$

This mode happens when the diodes conduction enlarges the phase interval of nonzero v_{ac} beyond the end of the conduction interval of the power switches, as exemplified in Fig. 8.

The overall waveform of the output voltage v_{ac} is similar to that considered in situation A about $v_{ac,ia}$, consequently, v_{ac} and θ_{ac} are given by (16) and (17). However, in this case the interval spanned by θ_{ia} ranges from an angle smaller than $-\pi/2$ to $-\pi$ so that the tip of $\overline{V}_{ac}$ lies on the limit arc instead that on the maximum arc.

The symmetry of phasor diagram with respect to the real axis holds also in this mode if $0 \leq \theta_{ia} \leq (\pi/2 - \alpha_a/2)$.

V. Phase Adjusting Property of PIVT

The phase adjusting property of the PIVT can be easily figured by conceiving an ideal experiment. Let us suppose that the equivalent loads at the HFI outputs are both resistive so that the phase displacements $\Delta\theta_{La}$ and $\Delta\theta_{Lb}$ between the output currents i_a and i_b and the relevant voltages $v_{ac,fa}$ and $v_{bc,fa}$ are zero. Then, there are no additional conduction intervals of the free-wheeling diodes and the phases θ_{vac} and θ_{vbc} of the output voltages with respect to $-v_{co,fa}$ are zero; being $\Delta\theta_{La} = \Delta\theta_{Lb} = 0$, the same holds also for θ_{ia}, and θ_{ib}.

If, for any reason, the equivalent load connected at the a-c output of the HFI becomes partially inductive, $\Delta\theta_{La}$ becomes negative. The lag of i_a with respect to $v_{ac,fa}$ originates additional conduction intervals for the diodes which, in turn, forces $v_{ac,fa}$ to lead $v_{bc,fa}$ of the phase angle $\theta_{\mathrm{vac}}>0$. Being understood that $\Delta\theta_{La}$ is dictated only by the equivalent load and is independent from θ_{vac}, the phase advance of $v_{ac,fa}$ shifts i_a forward of the same phase angle. Then, the resulting phase lag of i_a, with respect to $-v_{co,fa}$, equal to

$$\theta_{ia} = \Delta\theta_{La} + \theta_{vac} \quad (27)$$

is smaller than it would have been if θ_{vac} had remained equal to 0, thus reducing the phase displacement between i_a and i_b. This result holds even if $\Delta\theta_{La} > 0$, or if the reactive load is connected to the b-c output of the HFI. It is worth to highlight that the reactance of the equivalent load can arise from nonidealities of the WPTS, as hypothesized in the previous paragraphs, or from on-purpose designed compensation networks connected to the track coils or to the pickup. In both cases, the PIVT reduces the phase displacement between the HFI output currents with respect to the PST.

Equations (22) and (23), which hold in mode A, and (16) and (17), relevant to mode C, use θ_{ia} as independent variable to work out θ_{vac}, thus making difficult to apply directly (27) to obtain θ_{ia}. To circumvent this difficulty, it is useful to remind that usually the control algorithm of a WPTS generates the reference for the amplitude of i_a and manipulates V_{ac} adjusting α_a to track it. Thus, in the subsequent considerations V_{ac} is considered as a given parameter V_{ac}^* and θ_{ia} is computed as a function of both V_{ac}^* and $\Delta\theta_{La}$. As a byproduct of the procedure, α_a is obtained as well, showing that in some conditions there is not any α_a able to implement the required V_{ac}^*, thus finding the boundaries of the operating region where PIVT can be actually controlled.

The computation of θ_{ia} begins by hypothesizing that the PIVT is operating in mode A. Using (27) to express θ_{vac}, the components of $\overline{V}_{ac}$ are by definition equal to

$$\begin{cases} v_{ac,Re} = V_{ac}^* \cos(\theta_{ia} - \Delta\theta_{La}) \\ v_{ac,Im} = V_{ac}^* \sin(\theta_{ia} - \Delta\theta_{La}) \end{cases}. \tag{28}$$

The second of (28) can be expanded in

$$v_{ac,Im} = V_{ac}^* \left[\sin(\theta_{ia})\cos(\Delta\theta_{La}) - \cos(\theta_{ia})\sin(\Delta\theta_{La})\right]. \tag{29}$$

Equating (29) to the second of (21) it is possible to derive a relation between θ_{ia} and $\Delta\theta_{La}$ as

$$\theta_{ia} = \mathrm{atan}\left[\frac{\sin(\theta_{ia})}{\cos(\theta_{ia})}\right] = \mathrm{atan}\left[\frac{\sin(\Delta\theta_{La})}{\cos(\Delta\theta_{La}) + \frac{1}{2}\frac{V_M}{V_{ac}^*}}\right]. \tag{30}$$

Equation (30) states that $|\tan(\theta_{ia})|<|\tan(\Delta\theta_{La})|$ and that, consequently, $|\theta_{ia}|<|\Delta\theta_{La}|$, as expected. Moreover, (30) shows that for small values of V_{ac}^* the phase adjusting is more effective because $\mathrm{atan}(\theta_{ia})$ is small. If, instead, V_{ac}^* increases the phase adjusting is less effective.

Once θ_{ia} is obtained by (30), it is inserted in the first of (28) to compute $v_{ac,Re}$. Then, θ_{ia} and $v_{ac,Re}$ are used in the first of (21) to work out α_a in the form

$$\alpha_a = 2\mathrm{asin}\left(\frac{v_{ac,Re}}{V_M} + \frac{\cos(\theta_{ia})}{2} - \frac{1}{2}\right). \tag{31}$$

If $\alpha_a > 0$ and $(\alpha_a/2-\pi/2) < \theta_{ia} < 0$ the hypothesis of operating in condition A is verified and the values obtained from (30) and (31) are correct. Otherwise mode B is considered.

In mode B, the phasor $\overline{V}_{ac}$ is completely defined by α_a and so, being its amplitude V_{ac}^* given, by (25) it results

$$\alpha_a = 4\left[\mathrm{asin}\left(\frac{V_{ac}^*}{V_M}\right) - \frac{\pi}{4}\right]. \tag{32}$$

Once obtained α_a, it is substituted in (26) to find θ_{vac} and then, by (27) θ_{ia} is readily worked out. In this mode, α_a must be positive and θ_{ia} must satisfy the condition $(-\alpha_a/2 - \pi/2) \leq \theta_{ia} \leq (\alpha_a/2 - \pi/2)$, otherwise mode C is checked

In mode C, the actual output voltage cannot be controlled because it depends on the conduction of the diodes rather than on the power switches commands. From (17) and (27), θ_{ia} is computed as a function of the phase displacement due to the load obtaining

$$\theta_{ia} = 2\Delta\theta_{La} + \pi \tag{33}$$

then, using (16) and (17), $\overline{V}_{ac}$ is derived.

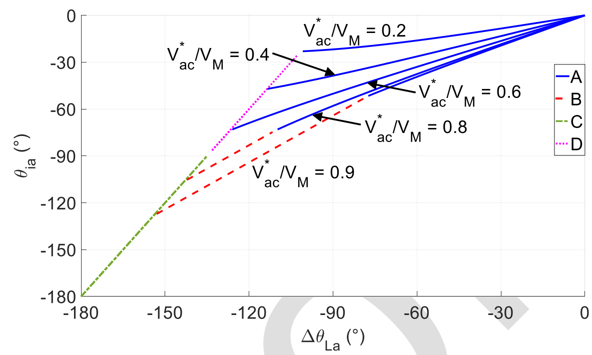

Fig. 9. Phase correction property of PIVT.

The phase displacement α_a can assume any value between 0 and $-2(\theta_{ia}$-$\pi/2)$ without affecting the PIVT functioning. If α_a exceeds the maximum value, then mode B occurs. Instead, if α_a is equal to 0 a particular case of mode A happens. This mode is denoted as D and its analysis is readily performed recognizing that (21) changes into (19), which in turn comes from (16) and (17). Then the PIVT functioning is described by (16), (17), and (33), like in mode C, but with the additional condition of having $\alpha_a = 0$.

Fig. 9 reports the plots of θ_{ia} as a function of $\Delta\theta_{La}$ for different values of the V_{ac}^*/V_M ratio. When $\Delta\theta_{La}$ is equal to zero, obviously θ_{ia} is equal to 0 as well, independently from the value of V_{ac}^*, and so all the curves begin at the origin of the graph. Initially PIVT operates in mode A and, according to (30), the phase compensation effect is stronger with small values of V_{ac}^*. This is reflected in Fig. 9, where the five different blue solid lines, each of them relevant to mode A with a different value of V_{ac}^*, show that for a given $|\Delta\theta_{\mathrm{La}}|$ the corresponding $|\theta_{ia}|$ is always smaller, and that their difference increases as V_{ac}^* decreases. As θ_{ia} becomes more negative, the contribution of the additional conduction intervals to the overall amplitude V_{ac} increases and α_a must be reduced to maintain V_{ac} equal to V_{ac}^*. At this point, two different evolutions are possible.

1) It happens that α_a must be set to zero while $|\theta_{ia}|<\pi/2$, passing to mode D. It is represented by the magenta dotted segment. If $\Delta\theta_{La}$ decreases further, the diodes conduction intervals enlarge even more and when their angular span exceeds $\pi/2$, mode C is enforced and the $(\Delta\theta_{La},\theta_{ia})$ pair moves on the green dash-dotted segment.
2) If V_{ac}^* is high enough, the enlarging diodes conduction intervals merge with the shrinking power switches conduction intervals before the latter ones reduce to zero, and originate situation B, represented by the red dashed lines. A further decrease of $\Delta\theta_{La}$ forces α_a to be set to zero, but now condition $|\theta_{ia}| > \pi/2$ holds and the PIVT moves from mode B to mode C without passing through mode D.

VI. PIVT Experimental Validation

A. Experimental Setup

The PIVT has been tested in an experimental setup that includes an HFI that supplies with the voltage v_{ac} the series-compensated coil "a" coupled with its pickup. The pickup

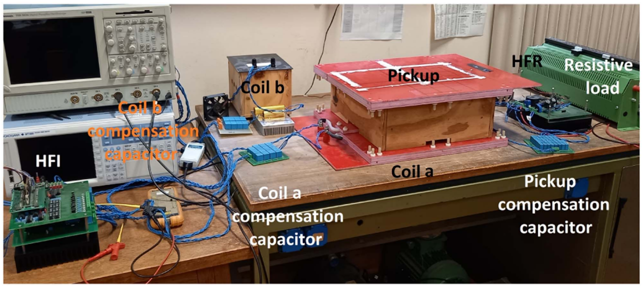

Fig. 10. Experimental setup.

TABLE I
WPTS CHARACTERISTICS

Parameter	Symbol	Value
Track coil, pickup, and inductor self-inductance	L_a, L_b, L_{pu}	120 μH
Resonant capacitor	$C_{a,N}$, $C_{b,N}$, $C_{p.u.,N}$	29 nF
Mutual inductance	M	30 μH
Supply angular frequency	ω	2π·85000 rad/s
Dc bus voltage	V_{dc}	200 V

is series-compensated as well, and is connected to an HFR formed by a diode H bridge. A capacitor is connected at the output of the HFR to smooth the oscillations of the dc bus voltage and a resistive load in parallel to the dc bus emulates the EV battery. The HFI output voltage v_{bc} supplies the coil "b" that is series-connected with a compensation capacitor and a resistive load. This arrangement emulates the behavior of another track coil, and maintains a constant resistive equivalent load at the HFI output in order to have i_b in phase to $v_{bc,fa}$ and to perform the tests in the same condition as considered in the previous Sections. Sizing and design of the HFI and its characteristics are described in details in [24]. Its power stage is based on the three-legs CCS050M12CM2 module manufactured by Wolfspeed and encompasses the driving and transduction circuitry. The control stage of the HFI was initially designed to drive only two legs of the power module and to implement the PST. It had been redesigned to drive the three legs of the power module and its control firmware, run by a Texas microcontroller TMS320F28335, has been rewritten to allow the implementation of the PIVT. The layout of the prototype is shown in Fig. 10 whilst Table I reports its main characteristics.

B. Experimental Tests and Results

A number of tests have been performed on the prototypal WPTS to check the ability of the PIVT of supplying two coils with different voltages and of reducing the effects of the reactance seen at the HFI output on the relative phases of the currents i_a and i_b. The tests have been performed by increasing step by step the capacitance of the resonant capacitor C_a connected to the coil "a" up to reaching twice its nominal value. The amplitude of both i_a and i_b has been maintained around 5A adjusting manually v_{ac} and v_{bc} acting on α_a and α_b. The samples of the quantities involved in each test have been acquired by means of a digital oscilloscope equipped with voltage and current probes.

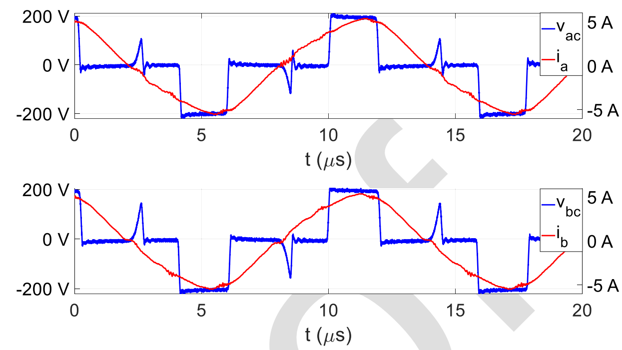

Fig. 11. HFI output voltages and currents with $C_a = C_{a,N}$.

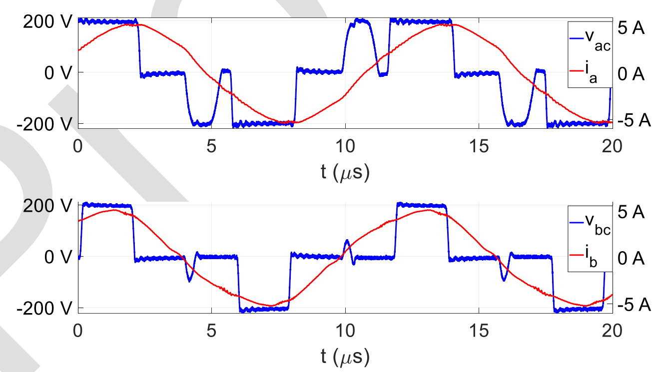

Fig. 12. HFI output voltages and currents with $C_a = 1.625{\cdot}C_{a,N}$.

In nominal conditions, i.e., when $C_a = C_{a,N}$ the voltages and the currents at the HFI outputs are those reported in Fig. 11. It can be seen that i_a and i_b are in phase because both the impedances seen at the inverter outputs are resistive. The spikes in the waveforms of v_{ab} and v_{bc} are due to the dead times of 0.5 μs inserted between the turning ~~OFF and ON~~ of the power switches of LGc.

The waveforms relevant to the test performed with $C_a = 1.625\ C_{a,N}$ are plotted in Fig. 12. The figure clearly shows the additional conduction intervals originated by the phase lag $\Delta\theta_{La}$ of i_a with respect to and v_{ac} and described in Section IV-A. These conduction intervals encompass also the spikes produced by the dead times, which instead are still visible in the waveform of v_{bc}. Now i_a and i_b are no more in phase but the additional voltage $v_{ac,ia}$ reduces the phase difference between the currents. The upper half of Fig. 13 shows the waveforms of the current i_{pk} in the pickup coil and of the voltage v_{pk} at the input of the HFR. Given that i_{pk} flows for the full supply period, each pair of the HFR diodes is in conduction and connects the dc bus to the input terminals of the HFR for half of the supply period thus explaining the square waveform of v_{pk}. The lower half of Fig. 13 reports the spectra of v_{ac} and i_a. They confirm what can be deduced by inspection of Figs. 11–12, i.e., that the current is nearly sinusoidal and that the approach based on the first harmonic components applied in the theoretical analysis performed in the previous sections is justified. Finally, Fig. 14 shows the waveforms of the voltages v_{an}, v_{bn}, and v_{cn} of the HFI, i.e.,

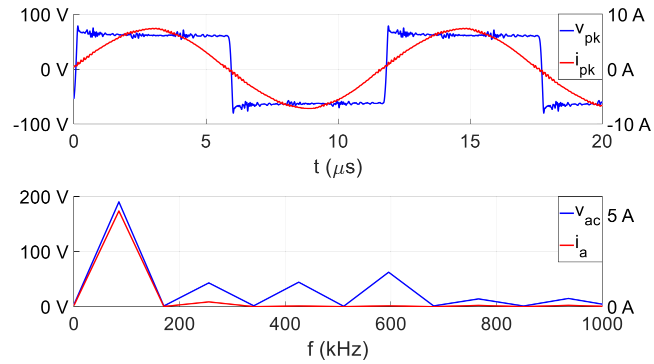

Fig. 13. Pickup voltage and current with $C_a = 1.625{\cdot}C_{a,N}$ (top). Spectra of v_{ac} and i_a (bottom).

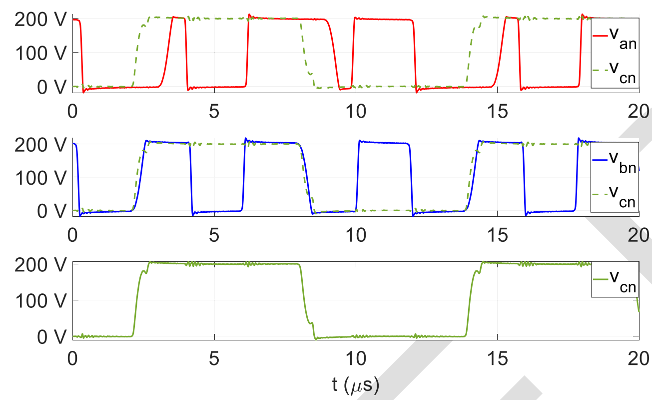

Fig. 14. HFI output voltages with $C_a = 1.625{\cdot}C_{a,N}$.

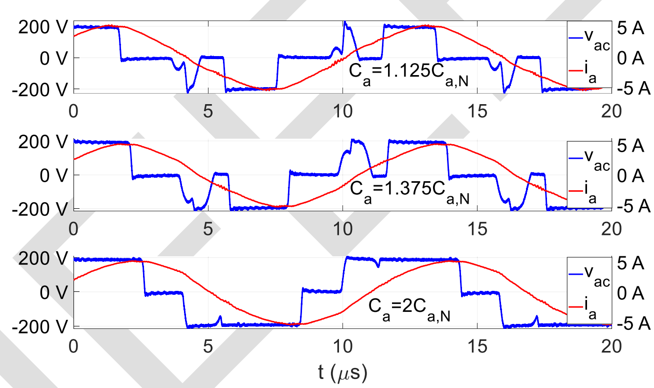

Fig. 15. HFI output voltages and current with $C_a = 1.25{\cdot}C_{a,N}$, $C_a = 1.5{\cdot}C_{a,N}$, and $C_a = 2C_{a,N}$.

the HFI output voltages referred to the negative terminal n of the dc bus. Apart for an offset of $V_{dc}/2$, they correspond with the expected profiles of v_{bo} and v_{co}, reported in Fig. 5, and of v_{ao}, plotted in Fig. 6.

Setting C_a to other different values does not affect the waveforms of v_{bc} and i_b and, hence, in Fig. 15 only v_{ac} and i_a are plotted. The figure confirms that the length of the conduction intervals increases together with the lag of i_a with respect to i_b. With $C_a = 2C_{a,N}$, the PIVT is near to pass to the B mode of operation.

TABLE II
EXPERIMENTAL RESULTS

$C_a/C_{a,n}$	θ_{ib} (°)	V_{ac}/V_M	$\Delta\theta_{La}$ (°)	θ_{ia} (°)	η_{PST}	η_{PIVT}
1.000	1.32	0.48	-2.14	-0.30	0.89	0.86
1.125	1.06	0.52	-20.70	-8.92	0.90	0.90
1.250	0.77	0.57	-32.45	-15.99	0.92	0.93
1.375	0.83	0.60	-40.00	-21.46	0.94	0.94
1.500	0.51	0.68	-45.24	-26.02	0.93	0.95
1.625	0.08	0.74	-49.23	-30.09	0.97	0.96
1.750	0.05	0.80	-52.05	-32.75	0.98	0.96
1.875	0.15	0.87	-54.21	-34.88	0.98	0.96
2.000	0.08	0.92	-56.21	-37.43	0.98	0.97

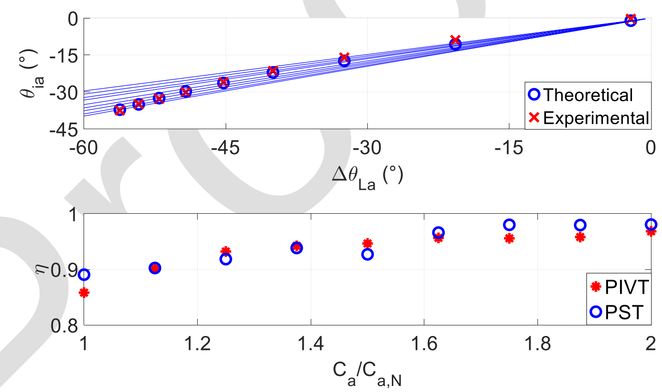

Fig. 16. Theoretical and experimental results comparison (top). Efficiency results (bottom).

The samples of the waveform relevant to v_{ac}, v_{bc}, i_a, and i_b have been processed by a MATLAB script to work out the amplitude and the phase of their first harmonic components obtaining the values listed in Table II. Following from the consideration of Sections II and III, if the load seen at the output b-c of the HFI is purely resistive, $v_{bc,fa}$ results in phase to $-v_{co,fa}$ and, hence, it has been used as phase reference for the other quantities instead of $-v_{co,fa}$ without impairing the results of the previous sections.

According to the second column of Table II, i_b results nearly perfectly in phase to $v_{bc,fa}$, thus confirming that the equivalent load at the b-c output of the HFI is actually resistive and that it is unaffected by the variation of C_a. The third column shows how V_{ac} has been increased to maintain a constant amplitude of i_a across the increasing impedance of the equivalent load. The fourth column reveals that $|\Delta\theta_{La}|$ never exceeds 60° and that consequently, according to Fig. 9, the PIVT always operate in mode A. The fifth column highlights the phase adjusting property of the PIVT that successes in reducing $|\theta_{ia}|$ with respect to $|\Delta\theta_{La}|$.

Equation (30) has been used to obtain the nine blue lines plotted in the upper half of Fig. 16. Each of them corresponds to one value of V_{ac}/V_M given in Table II and to $\Delta\theta_{La}$ spanning the interval $(-60°,0)$. As a matter of fact, Fig. 16 can be considered as a magnification of the upper-right part of Fig. 9. The blue circles are obtained inserting in (30) the (V_{ac}/V_M,$\Delta\theta_{La}$) pairs from Table II; each of them lies on a different line and represents the theoretical value of θ_{ia}. The red crosses, instead, correspond to the experimental value of θ_{ia}, reported on the fifth column of Table II.

Analysis of Fig. 16 shows that results from the experiments match very well with the expected ones and that PIVT is actually able to reduce the phase displacement between the currents when a reactive equivalent load is connected to the HFI outputs.

C. Efficiency Considerations

From the description given in Section III about the commutations of the power switches and of the diodes it derives that, with respect to the PST, the PIVT exhibits two additional zero-current commutations for each diode of LGa and LGb in each supply period. Other diode commutations happen at the turning ON and OFF of the power switches and are of the same type as those happening at the end of the dead times when the PST is used. Consequently, it can be concluded that the switching losses caused by the PIVT exceed those relevant to PST of the amount given by the zero-current commutation of the diodes. Moreover, in PIVT the diodes are flown by current for a comparatively long time so that their conduction losses should be considered whilst with the PST only the power switches are flown by current for most of the period.

The effect of the PIVT on the HFI efficiency have been explored by processing the samples of the input and output voltages and currents, acquired in the working conditions considered in Table II. The two last columns of the table report the average efficiency relevant to the PST and the PIVT. These quantities are plotted in the lower half of Fig. 16. Analysis of the data shows that at low values of $C_a/C_{a,N}$, the efficiency of PIVT is comparable with that of the PST whilst, for higher values of $C_a/C_{a,N}$, the PIVT performs a little worse. This behavior can be explained by supposing that the diodes switching losses do not affect much the overall efficiency of the HFI whilst it is more sensitive to the conduction losses of the diodes, which likely are higher than those of the power switches.

VII. Conclusion

This article proposes a modulation technique for a three-leg HFI that allows the simultaneous supply of two track coils of a WPTS. The amplitudes of the voltages supplying the two coils can be adjusted independently while maintaining the coil currents in phase for resistive HFI loads and reducing the current phase difference under the onset of a reactive component of the loads. The proposed technique has been deeply analyzed mathematically and then substantiated by experimental tests performed on a prototypal WPTS. The obtained results match very well with the expected ones. The efficiency measurement show that, adopting the proposed modulation technique, the losses of the HFI increases only marginally with respect to those of PST.

References

[1] S. Li and C. C. Mi, “Wireless power transfer for electric vehicle applications,” *IEEE J. Emerg. Sel. Topics Power Electron.*, vol. 3, no. 1, pp. 4–17, Mar. 2015.

[2] V. Cirimele, M. Diana, F. Freschi, and M. Mitolo, “Inductive power transfer for automotive applications: State-of-the-art and future trends,” *IEEE Trans. Ind. Appl.*, vol. 54, no. 5, pp. 4069–4079, Sep./Oct. 2018, doi: 10.1109/TIA.2018.2836098.

[3] R. Tavakoli and Z. Pantic, “Analysis, design, and demonstration of a 25-kW dynamic wireless charging system for roadway electric vehicles,” *IEEE J. Emerg. Sel. Topics Power Electron.*, vol. 6, no. 3, pp. 1378–1393, Sep. 2018.

[4] H. K. Dashora, G. Buja, M. Bertoluzzo, R. Pinto, and V. Lopresto, “Analysis and design of DD coupler for dynamic wireless charging of electric vehicles,” *J. Electromagn. Waves Appl.*, vol. 32, no. 2, pp. 170–189, 2018.

[5] G. Buja, M. Bertoluzzo, and H.K. Dashora, “Lumped track layout design for dynamic wireless charging of electric vehicles,” *IEEE Trans. Ind. Electron.*, vol. 63, no. 10, pp. 6631–6640, Oct. 2016.

[6] C. Cheng, Z. Zhou, W. Li, C. Zhu, Z. Deng, and C. C. Mi, “A multi-load wireless power transfer system with series-parallel-series compensation,” *IEEE Trans. Power Electron.*, vol. 34, no. 8, pp. 7126–7130, Aug. 2019, doi: 10.1109/TPEL.2019.2895598.

[7] Y. Wang, S. Zhao, H. Zhang, and F. Lu, “High-efficiency bilateral S–SP compensated multiload IPT system with constant-voltage outputs,” *IEEE Trans. Ind. Inform.*, vol. 18, no. 2, pp. 901–910, Feb. 2022, doi: 10.1109/TII.2021.3072394.

[8] L. Shuguang, Y. Zhenxing, and L. Wenbin, “Electric vehicle dynamic wireless charging technology based on multi-parallel primary coils,” in *Proc. IEEE Int. Conf. Electron. Commun. Eng.*, 2018, pp. 120–124.

[9] C. Wang, C. Zhu, K. Song, G. Wei, S. Dong, and R. G. Lu, “Primary-side control method in two-transmitter inductive wireless power transfer systems for dynamic wireless charging applications,” in *Proc. IEEE PELS Workshop Emerg. Technol., Wireless Power Transfer*, 2017, pp. 1–6.

[10] J. Zhao, Y. Zhang, and L. Qi, “Design and analysis of a flexible multi-output wireless power transfer system with variable inductor,” in *Proc. IEEE Energy Convers. Congr. Expo.*, 2021, pp. 1559–1564, doi: 10.1109/ECCE47101.2021.9595052.

[11] H. K. Dashora, M. Bertoluzzo, and G. Buja, “Reflexive properties for different pick-up circuit topologies in a distributed IPT track,” in *Proc. IEEE Int. Conf. Ind. Inform.*, 2015, pp. 69–75.

[12] M. Bertoluzzo, G. Buja, and H. Dashora, “Avoiding null power point in DD coils,” in *Proc. IEEE PELS Workshop Emerg. Technol., Wireless Power Transfer*, 2019, pp. 11–15.

[13] S. Huh and D. Ahn, “Two-transmitter wireless power transfer with optimal activation and current selection of transmitters,” *IEEE Trans. Power Electron.*, vol. 33, no. 6, pp. 4957–4967, Jun. 2018, doi: 10.1109/TPEL.2017.2725281.

[14] D.-H. Kim and D. Ahn, “Maximum efficiency point tracking for multiple-transmitter wireless power transfer,” *IEEE Trans. Power Electron.*, vol. 35, no. 11, pp. 11391–11400, Nov. 2020, doi: 10.1109/TPEL.2019.2919293.

[15] D.-H. Jang, “PWM methods for two-phase inverters,” *IEEE Ind. Appl. Mag.*, vol. 13, no. 2, pp. 50–61, Mar./Apr. 2007.

[16] Y. Zhang et al., “Free positioning wireless charging system based on tilted long-track transmitting coil array,” *IEEE Trans. Circuits Syst. II, Exp. Briefs*, vol. 69, no. 9, pp. 3849–3853, Sep. 2022, doi: 10.1109/TCSII.2022.3177617.

[17] SAE International, “Wireless power transfer for light-duty plug-in/electric vehicles and alignment methodology,” Oct. 2020. Accessed: Jun. 6, 2022. [Online]. Available: https://saemobilus.sae.org/content/J2954_202010/

[18] C. Carretero, O. Lucía, J. Acero, and J. M. Burdío, “Phase-shift control of dual half-bridge inverter feeding coupled loads for induction heating purposes,” *Electron. Lett.*, vol. 47, no. 11, pp. 670–671, May 2011.

[19] M. H. Rashid, *Power Electronics Circuits, Devices, and Applications*, 3rd ed. Englewood Cliffs, NJ, USA: Prentice-Hall, 2004.

[20] H. Dashora, M. Bertoluzzo, and G. Buja, “Dual-output inverter with phase correction ability for dynamic WPT track supply,” in *Proc. 45th Annu. Conf. IEEE Ind. Electron. Soc.*, 2019, pp. 6349–6354, doi: 10.1109/IECON.2019.8927534.

[21] W. Zhang and C.C. Mi, “Compensation topologies of high-power wireless power transfer systems,” *IEEE Trans. Veh. Technol.*, vol. 65, no. 6, pp. 4768–4778, Jun. 2016.

[22] U. Pratik, B. J. Varghese, A. Azad, and Z. Pantic, “Optimum design of decoupled concentric coils for operation in double-receiver wireless power transfer systems,” *IEEE J. Emerg. Sel. Topics Power Electron.*, vol. 7, no. 3, pp. 1982–1998, Sep. 2019, doi: 10.1109/JESTPE.2018.2871150.

[23] R. Mai, Y. Luo, B. Yang, Y. Song, S. Liu, and Z. He, “Decoupling circuit for automated guided vehicles IPT charging systems with dual receivers,” *IEEE Trans. Power Electron.*, vol. 35, no. 7, pp. 6652–6657, Jul. 2020, doi: 10.1109/TPEL.2019.2955970.

[24] G. Buja, M. Bertoluzzo, and K. N. Mude, “Design and experimentation of WPT charger for electric city car,” *IEEE Trans. Ind. Electron.*, vol. 62, no. 12, pp. 7436–7447, Dec. 2015, doi: 10.1109/TIE.2015.2455524.

Manuele Bertoluzzo received the M.S. degree in electronic engineering and the Ph.D. degree in industrial electronics and computer science from the University of Padova, Padova, Italy, in 1993 and 1997, respectively.

Since 2015, he has been an Associate Professor with the Department of Electrical Engineering, University of Padova and holds the lectureship of road electric vehicles and systems for automation. He is involved in analysis and design of power electronics systems, especially for wireless charging of electric vehicles battery.

Giuseppe Buja (Life Fellow, IEEE) received the “Laurea” degree (with hons.) in power electronics engineering from the University of Padova, Padova, Italy, in 1970.

He is currently a Senior Research Scientist with the University of Padova. He has carried out an extensive research work in the field of power and industrial electronics, originating the modulating-wave distortion and the optimum modulation for pulsewidth modulation inverters. His current research interests include automotive electrification, including wireless charging of electric vehicles, and grid-integration of renewable energies.

Hemant Kumar Dashora (Member, IEEE) received the B.E. degree from the University of Rajasthan, Jaipur, India, in 2009, and the M.Tech. degree from the Indian Institute of Technology Kharagpur, Kharagpur, India, in 2011, both in electrical engineering.

He was a Senior Engineer with the General Motors Technical Centre, Bangalore, India, for almost 3 years. He focused on modeling and simulation of a complete architecture of hybrid and electric vehicles to analyze their fuel economy, performance, and durability. His current research interests include dynamic wireless charging of electric vehicles, coupling coil, and power supply analysis.

Analysis and Experimentation of a Novel Modulation Technique for a Dual-Output WPT Inverter

Manuele Bertoluzzo, Giuseppe Buja, *Life Fellow, IEEE*, and Hemant Kumar Dashora, *Member, IEEE*

***Abstract*—Dynamic wireless power transfer systems require to supply many transmitting coils deployed under the road surface and arranged along the so-called track. This layout entails the use of a large number of inverters or of devices that switch the power to the proper coils. This article presents a technique that uses a single three-phase inverter to supply two coils with voltages having different and independently adjustable amplitudes of their first harmonic component. Differently from the well-known phase shift technique, the amplitude and the phase of the voltages are not correlated. Moreover, the presented technique has the ability of inherently reducing the phase difference between the two output currents when the supplied loads are partially reactive. This feature enhances the power transfer capability of the inverter when both the track coils are coupled with the same pickup. After presenting this technique, this article analyzes the functioning of the dual-output inverter in different load conditions recognizing the boundaries of four different modes of operation. For each of them the analytical expression of the amplitude and phase of the generated voltages are given. The theoretical findings are validated by experiments performed on a prototypal setup that implements the presented modulation technique.**

***Index Terms*—Inductive power transmission, phase control, voltage source inverters, wireless power transfer.**

I. Introduction

Wireless power transfer (WPT) based on magnetic induction is the subject of advanced studies that aim at transferring power onboard electric vehicles running on suitable tracks [1], [2], [3]. Implementation of tracks requires to design carefully the transmitting coils [4], their reciprocal placement [5], and their supply system. The latter one could include a large number of inverters and, hence, it is mandatory to optimize its architecture. Some proposals have been presented to minimize the complexity and the cost of the supply infrastructure by using only one inverter and relying on the interaction between the transmitting coils to transfer energy to a pickup coupled to any of them [6], [7]. With this arrangement, however, it is not possible to control independently the coils as all of them are always energized. Other approaches are based on switches that forward the power supplied by the inverter only to the track coils that must be energized; the switches are implemented by static devices [8], [9] or by additional inductors whose cores are on purpose saturated to control the power transfer [10]; another solution exploits the inherent variation of the impedance of the track coil coupled to the pickup to forward the supply power to it [11]. These approaches do not allow to control independently the power supplied to the energized coils and this could be a limiting factor if, depending on the distance between two subsequent track coils and on their dimension, the pickup is temporary coupled simultaneously with two of them [5]. In this case, both the track coils contribute to the power transfer, which is maximum when the currents flowing in the coils are in phase so as to sum the magnetic fluxes linked with the pickup. The same requirement is found also in [12], where the currents in the two subcoils of a track DD coil are controlled separately. Besides the phase relation between the currents, it is also important to control independently their amplitude to maximize the WPT system (WPTS) efficiency; Huh and Ahn [13] and Kim and Ahn [14] used separate inverters to supply the track coils, increasing the complexity of the infrastructure, and requiring to exchange some data between the inverters control stages [13] to synchronize the phases of the output currents.

A solution to reduce the cost and the complexity of the infrastructure is proposed in [15], where a PWM technique for a three-legs inverter with two outputs is presented. It allows to save two power switches with respect to the conventional solution of using two two-legs inverters. The same scheme is generalized in [16] for the supply of multiple track coils.

Considering that the surface vehicle standard J2954 issued by SAE [17] fixes to 85 kHz the nominal supply frequency f_s of the wireless charging stations, the PWM technique proposed in [15] is not viable to control the amplitude of the high frequency inverter (HFI) output voltage. Instead, in WPTSs, the phase shift technique (PST) is commonly used [18], [19], even if some authors propose to supply the transmitting coils with a square-wave voltage [16].

An original technique for the command of the HFI power switches has been presented in [20]. This technique is derived

Manuscript received 29 July 2022; revised 18 October 2022 and 7 November 2022; accepted 29 November 2022. *(Corresponding author: Manuele Bertoluzzo.)*

Manuele Bertoluzzo and Giuseppe Buja are with the Department of Industrial Engineering, University of Padova, 35131 Padova, Italy (e-mail: manuele.bertoluzzo@unipd.it; giuseppe.buja@unipd.it).

Hemant Kumar Dashora is with the KPIT Technologies Ltd., Pune 411057, India (e-mail: hemant.dashora@kpit.com).

Color versions of one or more figures in this article are available at https://doi.org/10.1109/TIE.2022.3227298.

Digital Object Identifier 10.1109/TIE.2022.3227298

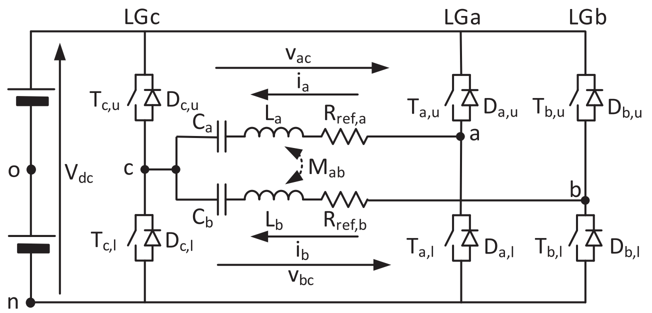

Fig. 1. Circuital scheme of the single output HFI (legs LGa and LGc) and of the dual output HFI (all the three legs).

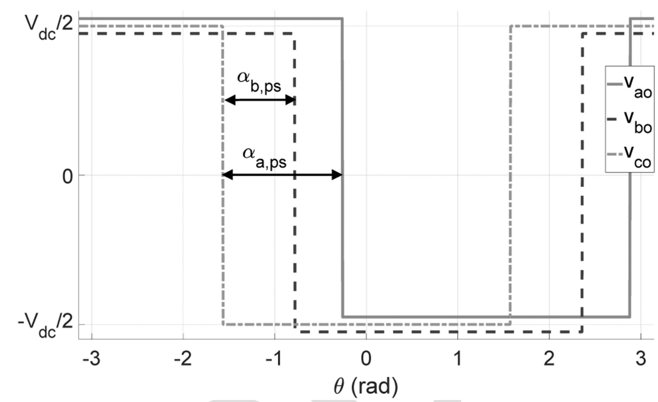

Fig. 2. Voltages v_{co}, v_{bo}, and v_{co} generated by PST.

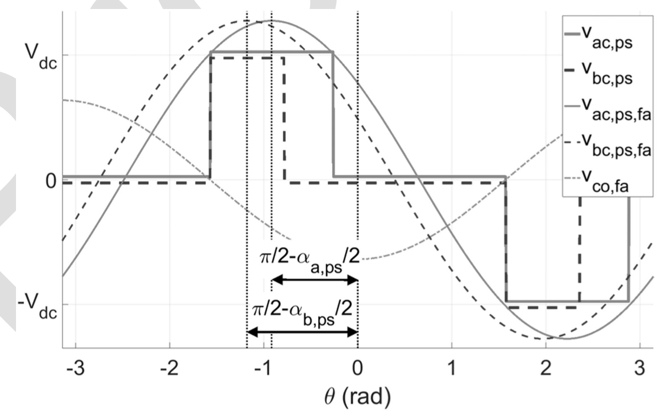

Fig. 3. Voltages $v_{ac,ps}$, $v_{bc,ps}$ and their first harmonic components generated by PST.

from the PST but, differently from it, allows to supply simultaneously two coils with two voltages whose amplitudes are adjusted independently while maintaining their phase relation. Moreover, when the loads seen at the HFI outputs are partially reactive, this technique exhibits the inherent ability of adjusting the phases of the output voltages in order to reduce the phase difference between the two output currents. With respect to [20], this article gives a much deeper mathematical analysis of the functioning and performance of the presented technique and, to this aim, uses the phasor notation to describe the generated voltages. The findings of the theoretical analysis are validated by the results of experimental tests.

The rest of this article is organized as follows. Section II reviews the functioning and the limitations of the PST and introduces the phasor representation used in the subsequent sections. Section III describes the proposed technique, and analyzes its operation with resistive loads. Section IV considers the effects of a partially reactive load on the amplitude and the phase of the output voltages. Section V demonstrates and quantifies the ability of the proposed technique to reduce the phase difference between the output currents. Section VI reports the results of the tests performed on a prototypal WPTS. Finally, Section VII concludes this article.

II. Phase Shift Technique

A. Conventional Phase Shift Technique

A single track coil can be supplied using an HFI formed by the two legs LGa and LGc sketched in Fig. 1. According to the PST, the power switches are commanded with square-wave gate signals to generate the two voltages v_{co} and v_{ao}. They can be expressed as

$$v_{co} = \text{ square}\left(\omega_s t + \frac{\pi}{2}\right) \quad (1)$$

$$v_{ao} = \text{ square}\left(\omega_s t + \frac{\pi}{2} - \alpha_{a,ps}\right) \quad (2)$$

where square(θ) is a square wave function having the falling edge at $\theta = 0$, $\omega_s = 2\pi{\cdot}f_s$ is the supply angular frequency and $\alpha_{a,ps}$ is the phase shift between the gate signals of the two legs. The voltages v_{co} and v_{ao} are plotted in Fig. 2 with the red solid line and the green dash-dotted line, respectively. In drawing the figure and in the subsequent discussion, the effects of the dead-times and of the finite commutation times are neglected. In this and in the following figures, a small offset is added to the square wave voltages in order to make it easier to distinguish them from each other.

The actual waveform of the output voltage v_{ac}, equal to

$$v_{ac,ps} = \ v_{ao} - v_{co} \quad (3)$$

is imposed by the phase shift $\alpha_{a,ps}$, which lies in the interval (0,π). When $\alpha_{a,ps} = 0$, v_{ao} is in phase with v_{co} and the output voltage $v_{ac,ps}$ is nullified; when $\alpha_{a,ps} = \pi$, v_{ao}, and v_{co} are in phase opposition and $v_{ac,ps}$ has a square waveform with twice the amplitude of v_{ao} and v_{co}. In general, $v_{ac,ps}$ has the three-level waveform shown by the red solid line in Fig. 3. In each semi period the length of the phase interval with nonzero voltage is equal to $\alpha_{a,ps}$.

Usually the coils of a WPTS are connected to suitable compensation networks made of reactive elements [21]. In Fig. 1, the compensation network of the coil a is formed by the series capacitor C_a that resonates with the coil inductance L_a. The impedance $R_{ref,a}$ accounts for the coil parasitic resistance and the equivalent load of the pickup side of the WPTS reflected to the transmitting side. If the series resonance is enforced at the pickup side, $R_{ref,a}$ results purely resistive.

The series resonant compensation introduces a minimum of the reactance seen at the inverter output in correspondence with the supply frequency. Consequently, the inverter output current is nearly sinusoidal despite the quasi-square waveform of the output voltage. From this condition it derives that the power transferred to the pickup is mainly dependent on the first harmonic component of the supply voltage and is only marginally affected by its higher order harmonics. For this reason, it is a common practice in the analysis of the WPTSs to consider only the first harmonic component of the output voltage rather than its actual waveform. The first harmonic component $v_{ac,ps,fa}$ of $v_{ac,ps}$ is expressed by

$$v_{ac,ps,fa} = \; V_{ac,ps} \;\; \cos\left(\omega_s t + \theta_{vac,ps}\right) \tag{4}$$

and is plotted in Fig. 3 using the thin red solid line.

Its amplitude $V_{ac,ps}$ is

$$V_{ac,ps} = \; V_{dc}\tfrac{4}{\pi} \;\; \sin\left(\frac{\alpha_{a,ps}}{2}\right) \triangleq \; V_M \;\; \sin\left(\frac{\alpha_{a,ps}}{2}\right) \tag{5}$$

where V_M is the maximum amplitude achievable by first harmonic component of the inverter output voltage with the given dc side voltage V_{dc}. The initial phase $\theta_{\mathrm{vac},ps}$ is measured with respect to the central point of the negative half period of v_{co} and results

$$\theta_{vac,ps} = \frac{\pi}{2} - \frac{\alpha_{a,ps}}{2}. \tag{6}$$

The simultaneous supply of two or more track coils can be performed using independent HFIs, however, it is possible to reduce the cost and the complexity of the WPTS by arranging the coils into pairs and supplying each pair using a three-legs HFI, as shown in Fig. 1. In this way, the power switches of the legs LGa and LGb are flown by the currents i_a and i_b, while LGc sustains the current i_c, equal to the sum of i_a and i_b.

Applying the PST with the phase shift angle $\theta_{b,ps}$ to the gate command of LGb and LGc, $v_{bc,ps}$ is obtained at the second output of the HFI according to

$$v_{bc,ps} = \; v_{bo} - \; v_{co} \;\; . \tag{7}$$

The amplitude V$_{bc,ps}$ of its first harmonic component can be adjusted independently from $V_{ac,ps}$, but, following from (6), if the phase shift angle $\alpha_{b,ps}$ differs from $\alpha_{a,ps}$, the phase $\theta_{vbc,ps}$ results different from $\theta_{\mathrm{vac},ps}$, as shown in Fig. 3 using the thin blue dashed line.

In the hypothesis that the reflected load is substantially resistive for both the track coils, as it usually happens when series compensation is used in the pickup, a phase displacement between the supply voltages entails an about equal phase displacement between i_a and i_b, thus impairing the power transfer capability of the WPTS when the two track coils supply the same pickup.

B. Phasor Representation of the Generated Voltages

To represent with more effectiveness the differences between the PST and the proposed technique, the phasor notation is introduced. Given the phase reference used in (4) and (6), the real axis of the phasor diagram corresponds to the opposite of the phasor of the first harmonic components $v_{co,fa}$ of v_{co}, represented in Fig. 3 using the thin green dash-dotted line.

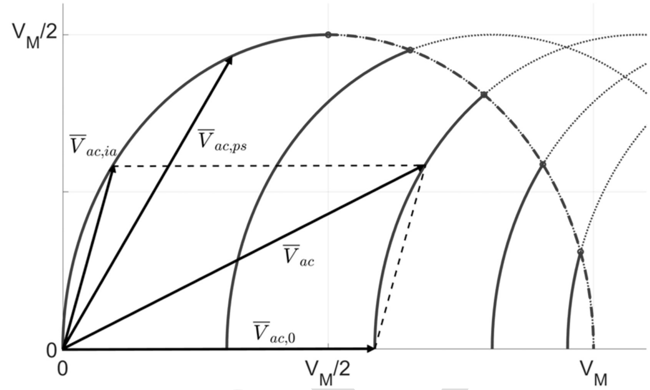

Fig. 4. Phasor representation of the output voltage.

The phasor of $v_{ac,ps,fa}$ is denoted as $\overline{V}_{ac,ps}$. Its components are derived from (5) and (6) with some manipulations that involve the use of the double-angle and the half-angle formulas

$$\begin{cases} v_{ac,ps,Re} = \; \frac{V_M}{2}\left(1 - \cos\left(\alpha_{a,ps}\right)\right) \\ v_{ac,ps,Im} = \; \frac{V_M}{2} \;\; \sin\left(\alpha_{a,ps}\right) \end{cases} . \tag{8}$$

By expressing $v^2_{ac,ps,Im}$ as a function of $v^2_{ac,ps,Re}$ and $v_{ac,ps,Re}$, the relation (9) is obtained

$$v^2_{ac,ps,Im} + \left(v_{ac,ps,Re} - \frac{V_M}{2}\right)^2 = \left(\frac{V_M}{2}\right)^2. \tag{9}$$

Equations (8) and (9) reveal that while $\alpha_{a,ps}$ spans the interval (0,π), the tip of $\overline{V}_{ac,ps}$ moves from (0,0) to (V_M,0) along the semi-circumference centered in (V_M/2,0) and having radius equal to V_M/2, as shown in Fig. 4.

III. Partially Imposed Voltage Technique

The modulation technique presented in [20] is based on the hypothesis that the currents supplied by the dual-output HFI flow for the full supply period, as it usually happens when the WPTS operates in resonance. This technique allows to adjust independently the amplitudes V_{ac} and V_{bc} while maintaining the phase relation

$$\theta_{vac} - \theta_{vbc} = 0. \tag{10}$$

In the same way as PST, the power switches of LGc are commanded with a 50% duty cycle, so that the voltage v_{co}, represented by the thick green dash-dotted line in the upper half of Fig. 5, is imposed during the full supply period. Differently from PST, there are not negligible intervals of the supply period during which neither the upper nor the lower switches of LGa and/or LGb are closed. In these intervals, the actual voltages v_{ao} and v_{bo} are not imposed by the switching commands but are dictated by the currents at the HFI outputs, which force the conduction of either the upper or the lower free-wheeling diodes. For this reason, the presented technique is designed as partially imposed voltage technique (PIVT).

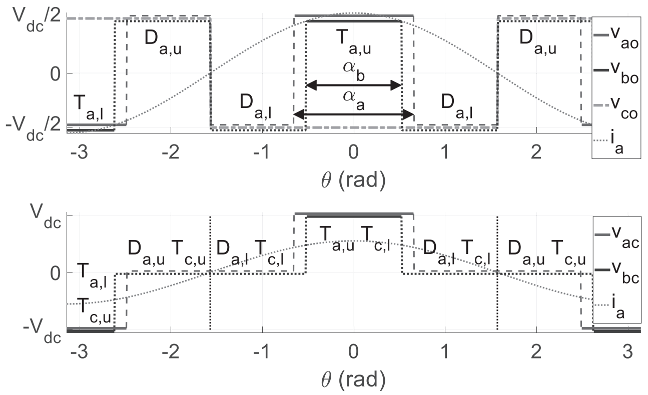

Fig. 5. Voltage waveforms generated by PIVT with $\theta_{ia} = \theta_{ib} = 0$.

More in details, as shown in the upper half of Fig. 5, the PIVT closes the upper switch $\mathrm{T_{a,u}}$ of LGa only for an interval centered around 0 and spanning α_a radians, and the lower switch $\mathrm{T_{a,l}}$ of the same leg for an equal interval centered around π. Consequently, the power switches of LGa are turned ON and OFF one time per supply period, like it happens in PST. While $\mathrm{T_{a,u}}$ or $\mathrm{T_{a,l}}$ are closed, the voltage v_{ao} is equal to V_{dc} or to $-V_{dc}$, respectively, as highlighted by the thick red solid line. When both the power switches are open, in agreement with the conventions of Fig. 1, at the positive zero crossing of current i_a, the upper freewheeling diode $\mathrm{D_{a,u}}$ of LGa is forced to turn OFF while the lower freewheeling diode $\mathrm{D_{a,l}}$ is forced to turn ON, driving v_{ao} to $-V_{dc}$. At the negative zero crossing of i_a, $\mathrm{D_{a,u}}$ is forced to turn ON, $\mathrm{D_{a,l}}$ is forced to turn OFF, and v_{ao} is driven to V_{dc}. When $\mathrm{T_{a,u}}$ is turned ON and OFF, $\mathrm{D_{a,l}}$ is forced to turn OFF and ON, respectively. The same happens with the pair $\mathrm{T_{a,l}}$-$\mathrm{D_{a,u}}$.

If i_a is in phase to $-v_{co,fa}$, as exemplified by the magenta dotted line of Fig. 5, the waveform of v_{ao} results as reported in the upper half of the figure, where the voltages due to the diode conduction are represented by the thin red dashed line. The output voltage $v_{ac} = v_{ao} - v_{co}$ is plotted in the lower half of Fig. 5, using the thick red solid line when the voltage is imposed by the power switches and the thin red dashed line when it is driven by the diodes. Obviously, PIVT is used also to command the power switches of LGb. If the current i_b is in phase to $-v_{co,fa}$, the voltages v_{bo} and v_{bc} have the waveforms plotted with the blue lines, the difference with respect to v_{ao} and v_{ac} being that the length of the power switches conduction intervals is α_b instead of α_a.

The waveforms of v_{ac} and v_{bc} are the same obtained with the PST but their phase is different as they are symmetric with respect to $\theta = 0$. Thanks to this symmetry, it results

$$\theta_{vac} = \theta_{vbc} = 0 \tag{11}$$

for any pair of α_a and α_b so that (10) is always verified. By (11), the two voltages result in phase to $-v_{co,fa}$ and, hence, they are in phase to i_a and i_b.

Equation (5) holds also for the amplitude of the first harmonic components of v_{ac} and v_{bc}. For v_{ac}, it is rewritten as

$$V_{ac,0} = V_M \sin\left(\frac{\alpha_a}{2}\right) \tag{12}$$

where the subscript "0" denotes that (12) refers to the condition of having i_a in phase to $v_{ac,fa}$. A similar relation holds also for $V_{bc,0}$ provided that α_b is used instead of α_a.

The components of $\overline{V}_{ac,0}$ are

$$\begin{cases} v_{ac,0,Re} = & V_M \ sin\left(\frac{\alpha_a}{2}\right) \\ v_{ac,0,Im} = & 0 \end{cases} \tag{13}$$

and while α_a varies in (0,π), the tip of the phasor $\overline{V}_{ac,0}$ moves from (0,0) to (V_M,0) along the real axis of Fig. 4.

The results of this section can be summarized by stating that if the loads seen at the HFI outputs are purely resistive, the currents i_a and i_b are in phase each to the other irrespectively from the relevant output voltages.

IV. Effect of Load Reactance

Generally speaking, if the track coils are coupled each other with the mutual inductance M_{ab} and with the pickup with the mutual inductances M_{ap} and M_{bp}, the expressions that link the supply voltages to the track coils currents are

$$\begin{cases} \overline{V}_{ac} = \left(\dot{Z}_a + \frac{\omega_s^2 M_{ap}^2}{\dot{Z}_p}\right)\bar{I}_a + \left(j\omega_s M_{ab} + \frac{\omega_s^2 M_{ap} M_{bp}}{\dot{Z}_p}\right)\bar{I}_b \\ \overline{V}_{bc} = \left(\dot{Z}_b + \frac{\omega_s^2 M_{bp}^2}{\dot{Z}_p}\right)\bar{I}_b + \left(j\omega_s M_{ab} + \frac{\omega_s^2 M_{ap} M_{bp}}{\dot{Z}_p}\right)\bar{I}_a \end{cases} \tag{14}$$

where $\dot{Z}_a$ and $\dot{Z}_b$ are the impedances of the assemblies made of the track coils and their compensation networks whilst $\dot{Z}_p$ is the impedance that accounts for the pickup, its compensation network and the load reflected at the input of the high frequency rectifier (HFR) that conditions the voltage induced across the pickup.

While the mutual inductance $\mathrm{M_{ab}}$ can be reduced by properly designing the coils [22] or by setting up a proper decoupling solution [23], the track coils interaction due to the coupling with the pickup cannot be avoided if both of them supply it at the same time. However, if the track coils and the pickup are series-compensated, the three impedances $\dot{Z}_a$, $\dot{Z}_b$, and $\dot{Z}_p$ are purely resistive and if $\overline{V}_{ac}$ and $\overline{V}_{ac}$ are in-phase, the same happens also for the currents.

The hypothesis of having purely resistive impedances $\dot{Z}_a$, $\dot{Z}_b$, and $\dot{Z}_p$ cannot be assured in practical application because of the tolerance on the components of the compensation networks, their variations with ageing, the dependence of the self-inductances and mutual inductance of the track coils and of the pickup to their relative positions.

Any of these causes originates a phase displacement between the currents i_a and i_b and the first harmonic components $v_{ac,fa}$ and $v_{bc,fa}$ of the relevant HFI output voltages. In the subsequent analysis it is supposed that the phase displacement can take any value even if, in a practical application, only the interval ($-\pi$/2,π/2) should be considered, otherwise the power would flow back from the load to the dc side of the HFI. In order to simplify the discussion, only the effect of a phase lag of i_a with respect to $-v_{co,fa}$ will be considered, with the awareness that the results can be easily adapted to the case of i_a leading $-v_{co,fa}$, and extended to the current i_b. Moreover, it is also supposed that $\alpha_a > 0$ whilst the generalization of the results to the case $\alpha_a = 0$ is reported in the next Section.

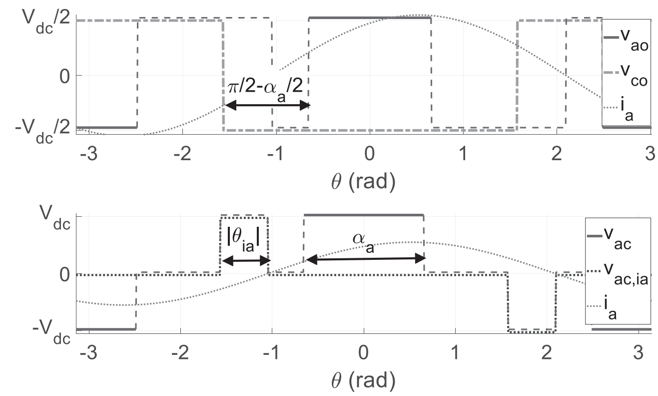

Fig. 6. Voltage waveforms generated by PIVT in mode A.

By analysis of Fig. 5, three modes of operation can be recognized: a) i_a changes its sign from negative to positive before $T_{a,u}$ is switched ON; b) i_a changes sign while $T_{a,u}$ is ON; c) i_a changes its sign after $T_{a,u}$ is switched OFF.

Each mode originates a different behavior and must be studied separately. In all the cases i_a is considered sinusoidal and is expressed as

$$i_a = I_a \cos\left(\omega_s t + \theta_{ia}\right). \tag{15}$$

A. $(\alpha_a/2 - \pi/2) < \theta_{ia} < 0$

This situation is exemplified in Fig. 6. By comparison with Fig. 5, it results that there are two more phase intervals where the HFI output voltage v_{ac} is different from zero. During the first interval, which begins at the falling edge of v_{co} and extends for a phase interval equal to $|\theta_{ia}|$, i_a maintains the conduction of $D_{a,u}$ so that v_{ac} results equal to V_{dc}. During the second interval, which has the same phase length and begins at the rising edge of v_{co}, the conducting diode is $D_{a,l}$ and v_{ac} is equal to $-V_{dc}$.

The voltage v_{ac} can be expressed as the sum of the output voltage plotted in Fig. 5 and relevant to the case of $\theta_{ia} = 0$, and of the voltage $v_{ac,ia}$, plotted with the blue dotted line in the lower half of Fig. 6, which includes only the two additional conduction intervals originated by the reactive component of i_a. The waveform of $v_{ac,ia}$ is similar to that of Fig. 3 and, hence, the parameters of its first harmonic components $v_{ac,ia,fa}$ are easily derived from (5) and (6) as

$$V_{ac,ia} = -V_M \sin\left(\frac{\theta_{ia}}{2}\right) \tag{16}$$

$$\theta_{vac,ia} = \frac{\pi}{2} + \frac{\theta_{ia}}{2} \tag{17}$$

where θ_{ia} is negative because, by hypothesis, $(\alpha_a/2 - \pi/2) < \theta_{ia} < 0$.

Equations (16) and (17) show that, differently from what happens with α_a, the angle θ_{ia} affects the phase of $v_{ac,ia,fa}$ besides its amplitude, and hence, it effects the phase of $v_{ac,fa}$.

The phasor of $v_{ac,fa}$ can be decomposed as in Fig. 4 in two contributes

$$\overline{V}_{ac} = \overline{V}_{ac,0} + \overline{V}_{ac,ia}. \tag{18}$$

The first of them is aligned with the real axis and has the components given by (13) while the components of $\overline{V}_{ac,ia}$, derived from (16) and (17) are

$$\begin{cases} v_{ac,ia,Re} = \frac{V_M}{2}\left(1 - \cos\left(\theta_{ia}\right)\right) \\ v_{ac,ia,Im} = -\frac{V_M}{2} \sin\left(\theta_{ia}\right). \end{cases} \tag{19}$$

From the comparison of (19) with (8) and by remembering that θ_{ia} is negative it can be concluded that the tip of $\overline{V}_{ac,ia}$ moves on the same semicircumference as the tip of $\overline{V}_{ac,ps}$. In the limit condition of $\alpha_a = 0$ and in the hypothesis that also in this case i_a flows for the full supply period, the constraint $(\alpha_a/2-\pi/2) < \theta_{ia} < 0$ states that θ_{ia} could span the interval $(-\pi/2,0)$ and that, consequently, the tip of $\overline{V}_{ac}$, which in this limit condition is equal to $\overline{V}_{ac,ia}$, would move on the arc of the semicircumference beginning at $(V_M/2, V_M/2)$ and ending at (0,0). This is denoted as the maximum arc.

In realistic operating conditions α_a is bigger than zero and as it increases, θ_{ia} can span a reducing angular interval so that the tip of $\overline{V}_{ac,ia}$ moves on shorter and shorter sections of the maximum arc, beginning at the point

$$\begin{cases} v_{ac,ia,Re,\max} = \frac{V_M}{2}\left(1 - \sin\left(\frac{\alpha_a}{2}\right)\right) \\ v_{ac,ia,Im,\max} = \frac{V_M}{2} \cos\left(\frac{\alpha_a}{2}\right) \end{cases} \tag{20}$$

and ending at (0,0). Equation (20) is obtained from (19) by setting $\theta_{ia} = -\pi/2 + \alpha_a/2$.

From (18), (19), and (13), the components of the phasor $\overline{V}_{ac}$ result

$$\begin{cases} v_{ac,Re} = \frac{V_M}{2}\left[2\sin\left(\frac{\alpha_a}{2}\right) + 1 - \cos\left(\theta_{ia}\right)\right] \\ v_{ac,Im} = -\frac{V_M}{2} \sin\left(\theta_{ia}\right) \end{cases} \tag{21}$$

from them, the amplitude and the phase of $\overline{V}_{ac}$ are readily derived as

$$V_{ac} = \frac{V_M}{2}\sqrt{\left[2\sin\left(\frac{\alpha_a}{2}\right) + 1 - \cos\left(\theta_{ia}\right)\right]^2 + \left[\sin\left(\theta_{ia}\right)\right]^2} \tag{22}$$

$$\theta_{vac,1} = a\tan\left[-\frac{\sin\left(\theta_{ia}\right)}{2\sin\left(\frac{\alpha_a}{2}\right) + 1 - \cos\left(\theta_{ia}\right)}\right]. \tag{23}$$

For a given value of α_a, V_{ac} results higher than $V_{ac,0}$ because of the contribute of $\overline{V}_{ac,ia}$, but in any case, V_{ac} never exceeds V_M, which is reached when $\alpha_a = \pi$ and $\overline{V}_{ac,ia}$ is null.

For any value of α_a in $(0,\pi)$, while θ_{ia} spans the interval $(\alpha_a/2-\pi/2,0)$, the tip of $\overline{V}_{ac}$ moves on an arc originating at

$$\begin{cases} v_{ac,Re,\max} = \frac{V_M}{2}\left(1 + \sin\left(\frac{\alpha_a}{2}\right)\right) \\ v_{ac,Im,\max} = \frac{V_M}{2} \cos\left(\frac{\alpha_a}{2}\right) \end{cases} \tag{24}$$

and ending at $(V_M \cdot \sin(\alpha_a/2), 0)$. The origins of these arcs lie on the quarter of circumference drawn with the blue dash-dotted line in Fig. 4. It is denoted as limit arc because, together the maximum arc, it bounds the semicircle where all the possible phasors $\overline{V}_{ac}$ fall.

Fig. 4 reports an example of the decomposition of $\overline{V}_{ac}$ according to (18) and all the possible positions of its tip for five different values of α_a. When $\alpha_a = 0$ the maximum arc on the left, expressed by (19), is obtained; as α_a increases the arcs

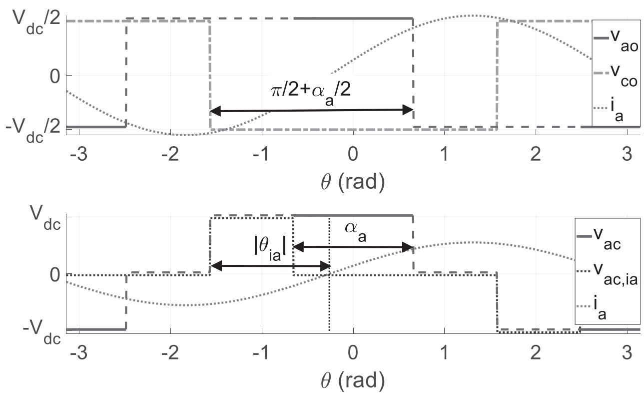

Fig. 7. Voltage waveforms generated by PIVT in mode B.

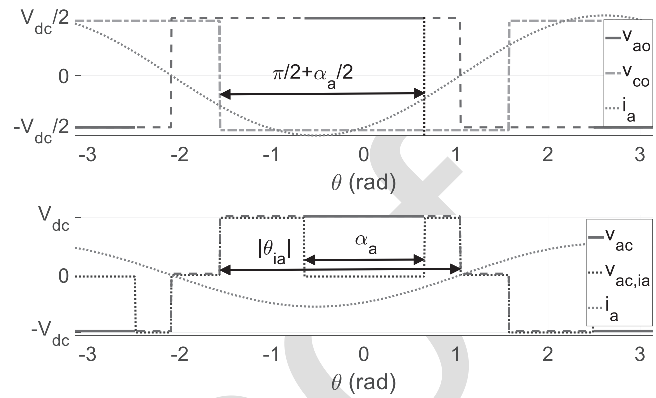

Fig. 8. Voltage waveforms generated by PIVT in mode C.

origins move to the right on the limit arc and the arcs length diminishes. Any two arcs intersect only outside the boundary semicircumference and, consequently, for any given phasor $\overline{V}_{ac}$ there is only one pair of α_a and θ_{ia} that realize it.

The analysis of the PIVT when i_a leads $-v_{co,fa}$ and $0 \leq \theta_{ia} \leq (\pi/2 - \alpha_a/2)$ is readily derived from the previous results considering that in this situation the conduction intervals of the diodes are on the right of the power switches conduction intervals instead that on the left. As a consequence, the phase of $\overline{V}_{ac,ia}$ is negative and the phasor diagram of Fig. 4 must be redrawn symmetrically with respect to the real axis.

B. $(-\alpha_a/2 - \pi/2) \leq \theta_{ia} \leq (\alpha_a/2 - \pi/2)$

This mode is exemplified in Fig. 7. By comparison with Fig. 6, it results that now the intervals of diode conduction extend up to the turning ON of the power switches. As a consequence, the output voltage v_{ac} results positive from $-\pi/2$ to α_a and negative from $\pi/2$ to $\pi+\alpha_a$ with a waveform that depends on α_a only, being the same that would have been obtained using the PST with $\alpha_{\mathrm{a,ps}} = \pi/2+\alpha_a/2$. The amplitude and the phase of $v_{\mathrm{ac,fa}}$ are then expressed by (25) and (26), obtained from (5) and (6)

$$V_{ac} = \ V_M \ \sin\left(\frac{\pi}{4} + \frac{\alpha_a}{4}\right) \tag{25}$$

$$\theta_{vac} = \frac{\pi}{4} - \frac{\alpha_a}{4}. \tag{26}$$

The components of $\overline{V}_{ac}$ are worked out manipulating (25) and (26) obtaining expressions equal to (24), thus demonstrating that while α_a spans the interval (0,π), the tip of $\overline{V}_{ac}$ lies on the limit arc.

As in the previous mode, if the current i_a leads $-v_{co,fa}$ and $(\pi/2 - \alpha_a/2) \leq \theta_{ia} \leq (\pi/2+\alpha_a/2)$, the findings are still valid provided that the diagram of Fig. 4 is redrawn symmetrically with respect to the real axis.

C. $-\pi \leq \theta_{ia} \leq (-\alpha_a/2 - \pi/2)$

This mode happens when the diodes conduction enlarges the phase interval of nonzero v_{ac} beyond the end of the conduction interval of the power switches, as exemplified in Fig. 8.

The overall waveform of the output voltage v_{ac} is similar to that considered in situation A about $v_{ac,ia}$, consequently, v_{ac} and θ_{ac} are given by (16) and (17). However, in this case the interval spanned by θ_{ia} ranges from an angle smaller than $-\pi/2$ to $-\pi$ so that the tip of $\overline{V}_{ac}$ lies on the limit arc instead that on the maximum arc.

The symmetry of phasor diagram with respect to the real axis holds also in this mode if $0 \leq \theta_{ia} \leq (\pi/2 - \alpha_a/2)$.

V. Phase Adjusting Property of PIVT

The phase adjusting property of the PIVT can be easily figured by conceiving an ideal experiment. Let us suppose that the equivalent loads at the HFI outputs are both resistive so that the phase displacements $\Delta\theta_{La}$ and $\Delta\theta_{Lb}$ between the output currents i_a and i_b and the relevant voltages $v_{ac,fa}$ and $v_{bc,fa}$ are zero. Then, there are no additional conduction intervals of the free-wheeling diodes and the phases θ_{vac} and θ_{vbc} of the output voltages with respect to $-v_{co,fa}$ are zero; being $\Delta\theta_{La} = \Delta\theta_{Lb} = 0$, the same holds also for θ_{ia}, and θ_{ib}.

If, for any reason, the equivalent load connected at the a-c output of the HFI becomes partially inductive, $\Delta\theta_{La}$ becomes negative. The lag of i_a with respect to $v_{ac,fa}$ originates additional conduction intervals for the diodes which, in turn, forces $v_{ac,fa}$ to lead $v_{bc,fa}$ of the phase angle $\theta_{\mathrm{vac}}>0$. Being understood that $\Delta\theta_{La}$ is dictated only by the equivalent load and is independent from θ_{vac}, the phase advance of $v_{ac,fa}$ shifts i_a forward of the same phase angle. Then, the resulting phase lag of i_a, with respect to $-v_{co,fa}$, equal to

$$\theta_{ia} = \Delta\theta_{La} \ + \theta_{vac} \tag{27}$$

is smaller than it would have been if θ_{vac} had remained equal to 0, thus reducing the phase displacement between i_a and i_b. This result holds even if $\Delta\theta_{La} > 0$, or if the reactive load is connected to the b-c output of the HFI. It is worth to highlight that the reactance of the equivalent load can arise from nonidealities of the WPTS, as hypothesized in the previous paragraphs, or from on-purpose designed compensation networks connected to the track coils or to the pickup. In both cases, the PIVT reduces the phase displacement between the HFI output currents with respect to the PST.

Equations (22) and (23), which hold in mode A, and (16) and (17), relevant to mode C, use θ_{ia} as independent variable to work out θ_{vac}, thus making difficult to apply directly (27) to obtain θ_{ia}. To circumvent this difficulty, it is useful to remind that usually the control algorithm of a WPTS generates the reference for the amplitude of i_a and manipulates V_{ac} adjusting α_a to track it. Thus, in the subsequent considerations V_{ac} is considered as a given parameter V_{ac}^* and θ_{ia} is computed as a function of both V_{ac}^* and $\Delta\theta_{La}$. As a byproduct of the procedure, α_a is obtained as well, showing that in some conditions there is not any α_a able to implement the required V_{ac}^*, thus finding the boundaries of the operating region where PIVT can be actually controlled.

The computation of θ_{ia} begins by hypothesizing that the PIVT is operating in mode A. Using (27) to express θ_{vac}, the components of $\overline{V}_{ac}$ are by definition equal to

$$\begin{cases} v_{ac,Re} = V_{ac}^* \cos\left(\theta_{ia} - \Delta\theta_{La}\right) \\ v_{ac,Im} = V_{ac}^* \sin\left(\theta_{ia} - \Delta\theta_{La}\right) \end{cases}. \tag{28}$$

The second of (28) can be expanded in

$$v_{ac,Im} = V_{ac}^* \left[\sin\left(\theta_{ia}\right)\cos\left(\Delta\theta_{La}\right) - \cos\left(\theta_{ia}\right)\sin\left(\Delta\theta_{La}\right)\right]. \tag{29}$$

Equating (29) to the second of (21) it is possible to derive a relation between θ_{ia} and $\Delta\theta_{La}$ as

$$\theta_{ia} = \mathrm{atan}\left[\frac{\sin\left(\theta_{ia}\right)}{\cos\left(\theta_{ia}\right)}\right] = \mathrm{atan}\left[\frac{\sin\left(\Delta\theta_{La}\right)}{\cos\left(\Delta\theta_{La}\right) + \frac{1}{2}\frac{V_M}{V_{ac}^*}}\right]. \tag{30}$$

Equation (30) states that $|\tan(\theta_{ia})| < |\tan(\Delta\theta_{La})|$ and that, consequently, $|\theta_{ia}| < |\Delta\theta_{La}|$, as expected. Moreover, (30) shows that for small values of V_{ac}^* the phase adjusting is more effective because atan(θ_{ia}) is small. If, instead, V_{ac}^* increases the phase adjusting is less effective.

Once θ_{ia} is obtained by (30), it is inserted in the first of (28) to compute $v_{ac,Re}$. Then, θ_{ia} and $v_{ac,Re}$ are used in the first of (21) to work out α_a in the form

$$\alpha_a = 2\mathrm{asin}\left(\frac{v_{ac,Re}}{V_M} + \frac{\cos\left(\theta_{ia}\right)}{2} - \frac{1}{2}\right). \tag{31}$$

If $\alpha_a > 0$ and $(\alpha_a/2 - \pi/2) < \theta_{ia} < 0$ the hypothesis of operating in condition A is verified and the values obtained from (30) and (31) are correct. Otherwise mode B is considered.

In mode B, the phasor $\overline{V}_{ac}$ is completely defined by α_a and so, being its amplitude V_{ac}^* given, by (25) it results

$$\alpha_a = 4\left[\mathrm{asin}\left(\frac{V_{ac}^*}{V_M}\right) - \frac{\pi}{4}\right]. \tag{32}$$

Once obtained α_a, it is substituted in (26) to find θ_{vac} and then, by (27) θ_{ia} is readily worked out. In this mode, α_a must be positive and θ_{ia} must satisfy the condition $(-\alpha_a/2 - \pi/2) \leq \theta_{ia} \leq (\alpha_a/2 - \pi/2)$, otherwise mode C is checked

In mode C, the actual output voltage cannot be controlled because it depends on the conduction of the diodes rather than on the power switches commands. From (17) and (27), θ_{ia} is computed as a function of the phase displacement due to the load obtaining

$$\theta_{ia} = 2\Delta\theta_{La} + \pi \tag{33}$$

then, using (16) and (17), $\overline{V}_{ac}$ is derived.

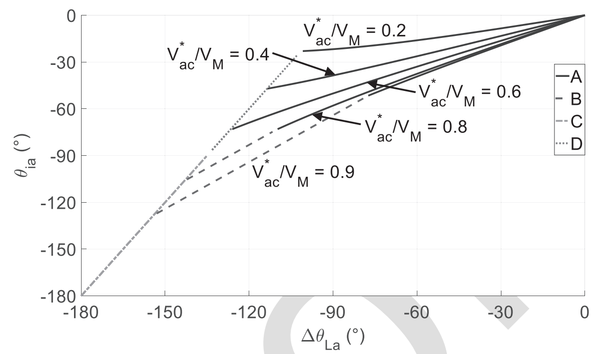

Fig. 9. Phase correction property of PIVT.

The phase displacement α_a can assume any value between 0 and $-2(\theta_{ia}$-$\pi/2)$ without affecting the PIVT functioning. If α_a exceeds the maximum value, then mode B occurs. Instead, if α_a is equal to 0 a particular case of mode A happens. This mode is denoted as D and its analysis is readily performed recognizing that (21) changes into (19), which in turn comes from (16) and (17). Then the PIVT functioning is described by (16), (17), and (33), like in mode C, but with the additional condition of having $\alpha_a = 0$.

Fig. 9 reports the plots of θ_{ia} as a function of $\Delta\theta_{La}$ for different values of the V_{ac}^*/V_M ratio. When $\Delta\theta_{La}$ is equal to zero, obviously θ_{ia} is equal to 0 as well, independently from the value of V_{ac}^*, and so all the curves begin at the origin of the graph. Initially PIVT operates in mode A and, according to (30), the phase compensation effect is stronger with small values of V_{ac}^*. This is reflected in Fig. 9, where the five different blue solid lines, each of them relevant to mode A with a different value of V_{ac}^*, show that for a given $|\Delta\theta_{\mathrm{La}}|$ the corresponding $|\theta_{ia}|$ is always smaller, and that their difference increases as V_{ac}^* decreases. As θ_{ia} becomes more negative, the contribution of the additional conduction intervals to the overall amplitude V_{ac} increases and α_a must be reduced to maintain V_{ac} equal to V_{ac}^*. At this point, two different evolutions are possible.

1) It happens that α_a must be set to zero while $|\theta_{ia}| < \pi/2$, passing to mode D. It is represented by the magenta dotted segment. If $\Delta\theta_{La}$ decreases further, the diodes conduction intervals enlarge even more and when their angular span exceeds $\pi/2$, mode C is enforced and the $(\Delta\theta_{La}, \theta_{ia})$ pair moves on the green dash-dotted segment.
2) If V_{ac}^* is high enough, the enlarging diodes conduction intervals merge with the shrinking power switches conduction intervals before the latter ones reduce to zero, and originate situation B, represented by the red dashed lines. A further decrease of $\Delta\theta_{La}$ forces α_a to be set to zero, but now condition $|\theta_{ia}| > \pi/2$ holds and the PIVT moves from mode B to mode C without passing through mode D.

VI. PIVT Experimental Validation

A. Experimental Setup

The PIVT has been tested in an experimental setup that includes an HFI that supplies with the voltage v_{ac} the series-compensated coil "a" coupled with its pickup. The pickup

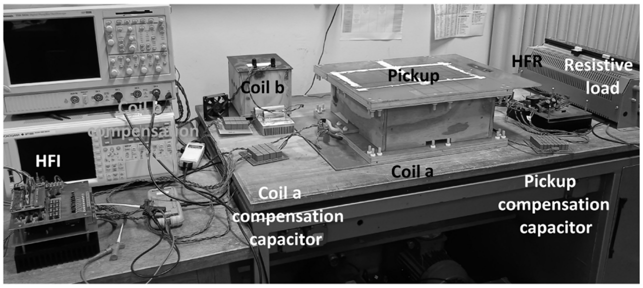

Fig. 10. Experimental setup.

TABLE I
WPTS CHARACTERISTICS

Parameter	Symbol	Value
Track coil, pickup, and inductor self-inductance	L_a, L_b, L_{pu}	120 μH
Resonant capacitor	$C_{a,N}$, $C_{b,N}$, $C_{p.u.,N}$	29 nF
Mutual inductance	M	30 μH
Supply angular frequency	ω	$2\pi\cdot 85000$ rad/s
Dc bus voltage	V_{dc}	200 V

is series-compensated as well, and is connected to an HFR formed by a diode H bridge. A capacitor is connected at the output of the HFR to smooth the oscillations of the dc bus voltage and a resistive load in parallel to the dc bus emulates the EV battery. The HFI output voltage v_{bc} supplies the coil "b" that is series-connected with a compensation capacitor and a resistive load. This arrangement emulates the behavior of another track coil, and maintains a constant resistive equivalent load at the HFI output in order to have i_b in phase to $v_{bc,fa}$ and to perform the tests in the same condition as considered in the previous Sections. Sizing and design of the HFI and its characteristics are described in details in [24]. Its power stage is based on the three-legs CCS050M12CM2 module manufactured by Wolfspeed and encompasses the driving and transduction circuitry. The control stage of the HFI was initially designed to drive only two legs of the power module and to implement the PST. It had been redesigned to drive the three legs of the power module and its control firmware, run by a Texas microcontroller TMS320F28335, has been rewritten to allow the implementation of the PIVT. The layout of the prototype is shown in Fig. 10 whilst Table I reports its main characteristics.

B. Experimental Tests and Results

A number of tests have been performed on the prototypal WPTS to check the ability of the PIVT of supplying two coils with different voltages and of reducing the effects of the reactance seen at the HFI output on the relative phases of the currents i_a and i_b. The tests have been performed by increasing step by step the capacitance of the resonant capacitor C_a connected to the coil "a" up to reaching twice its nominal value. The amplitude of both i_a and i_b has been maintained around 5A adjusting manually v_{ac} and v_{bc} acting on α_a and α_b. The samples of the quantities involved in each test have been acquired by means of a digital oscilloscope equipped with voltage and current probes.

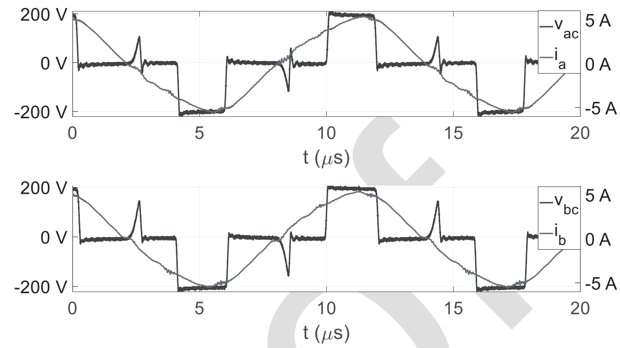

Fig. 11. HFI output voltages and currents with $C_a = C_{a,N}$.

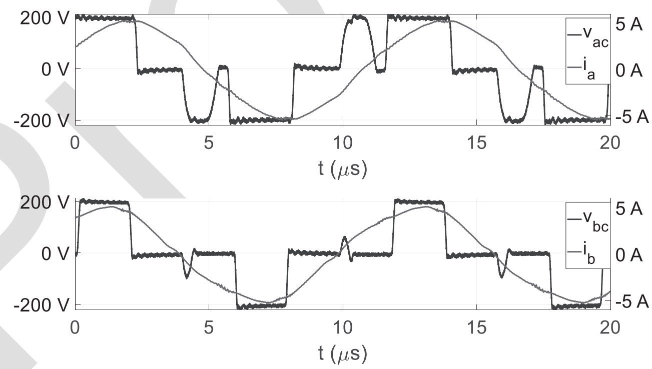

Fig. 12. HFI output voltages and currents with $C_a = 1.625 \cdot C_{a,N}$.

In nominal conditions, i.e., when $C_a = C_{a,N}$ the voltages and the currents at the HFI outputs are those reported in Fig. 11. It can be seen that i_a and i_b are in phase because both the impedances seen at the inverter outputs are resistive. The spikes in the waveforms of v_{ab} and v_{bc} are due to the dead times of 0.5 μs inserted between the turning OFF and ON of the power switches of LGc.

The waveforms relevant to the test performed with $C_a = 1.625\ C_{a,N}$ are plotted in Fig. 12. The figure clearly shows the additional conduction intervals originated by the phase lag $\Delta\theta_{La}$ of i_a with respect to and v_{ac} and described in Section IV-A. These conduction intervals encompass also the spikes produced by the dead times, which instead are still visible in the waveform of v_{bc}. Now i_a and i_b are no more in phase but the additional voltage $v_{ac,ia}$ reduces the phase difference between the currents. The upper half of Fig. 13 shows the waveforms of the current i_{pk} in the pickup coil and of the voltage v_{pk} at the input of the HFR. Given that i_{pk} flows for the full supply period, each pair of the HFR diodes is in conduction and connects the dc bus to the input terminals of the HFR for half of the supply period thus explaining the square waveform of v_{pk}. The lower half of Fig. 13 reports the spectra of v_{ac} and i_a. They confirm what can be deduced by inspection of Figs. 11–12, i.e., that the current is nearly sinusoidal and that the approach based on the first harmonic components applied in the theoretical analysis performed in the previous sections is justified. Finally, Fig. 14 shows the waveforms of the voltages v_{an}, v_{bn}, and v_{cn} of the HFI, i.e.,

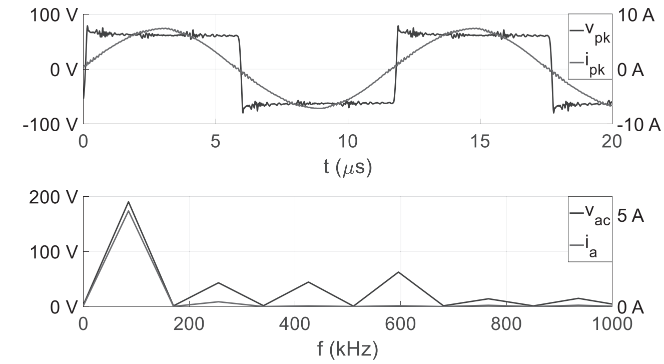

Fig. 13. Pickup voltage and current with $C_a = 1.625 \cdot C_{a,N}$ (top). Spectra of v_{ac} and i_a (bottom).

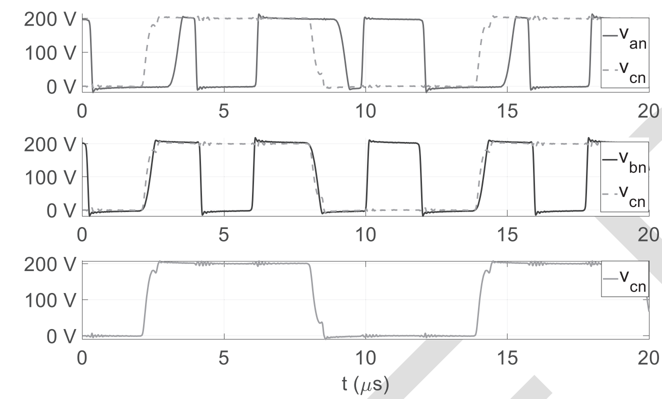

Fig. 14. HFI output voltages with $C_a = 1.625 \cdot C_{a,N}$.

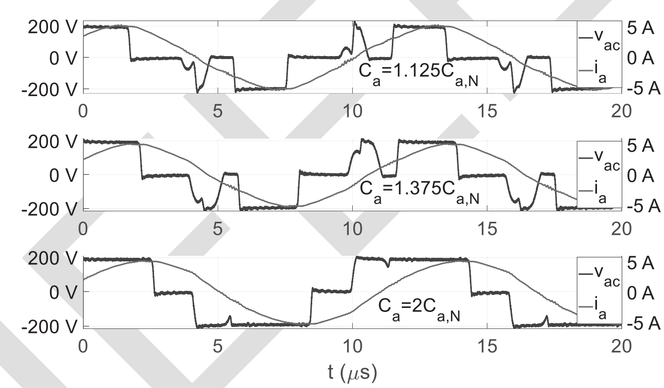

Fig. 15. HFI output voltages and current with $C_a = 1.25 \cdot C_{a,N}$, $C_a = 1.5 \cdot C_{a,N}$, and $C_a = 2C_{a,N}$.

the HFI output voltages referred to the negative terminal *n* of the dc bus. Apart for an offset of $V_{dc}/2$, they correspond with the expected profiles of v_{bo} and v_{co}, reported in Fig. 5, and of v_{ao}, plotted in Fig. 6.

Setting C_a to other different values does not affect the waveforms of v_{bc} and i_b and, hence, in Fig. 15 only v_{ac} and i_a are plotted. The figure confirms that the length of the conduction intervals increases together with the lag of i_a with respect to i_b. With $C_a = 2C_{a,N}$, the PIVT is near to pass to the B mode of operation.

TABLE II
EXPERIMENTAL RESULTS

$C_a/C_{a,n}$	θ_{ib} (°)	V_{ac}/V_M	$\Delta\theta_{La}$ (°)	θ_{ia} (°)	η_{PST}	η_{PIVT}
1.000	1.32	0.48	-2.14	-0.30	0.89	0.86
1.125	1.06	0.52	-20.70	-8.92	0.90	0.90
1.250	0.77	0.57	-32.45	-15.99	0.92	0.93
1.375	0.83	0.60	-40.00	-21.46	0.94	0.94
1.500	0.51	0.68	-45.24	-26.02	0.93	0.95
1.625	0.08	0.74	-49.23	-30.09	0.97	0.96
1.750	0.05	0.80	-52.05	-32.75	0.98	0.96
1.875	0.15	0.87	-54.21	-34.88	0.98	0.96
2.000	0.08	0.92	-56.21	-37.43	0.98	0.97

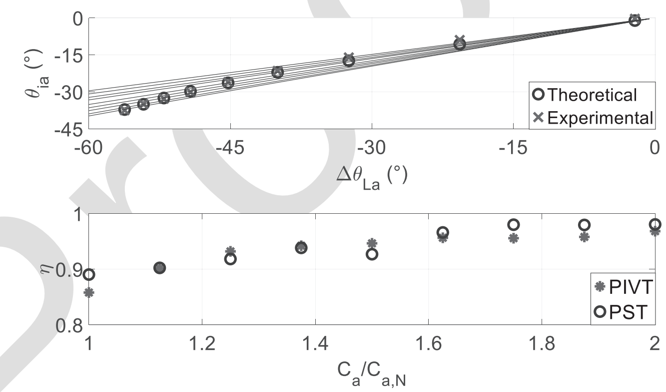

Fig. 16. Theoretical and experimental results comparison (top). Efficiency results (bottom).

The samples of the waveform relevant to v_{ac}, v_{bc}, i_a, and i_b have been processed by a MATLAB script to work out the amplitude and the phase of their first harmonic components obtaining the values listed in Table II. Following from the consideration of Sections II and III, if the load seen at the output b-c of the HFI is purely resistive, $v_{bc,fa}$ results in phase to $-v_{co,fa}$ and, hence, it has been used as phase reference for the other quantities instead of $-v_{co,fa}$ without impairing the results of the previous sections.

According to the second column of Table II, i_b results nearly perfectly in phase to $v_{bc,fa}$, thus confirming that the equivalent load at the b-c output of the HFI is actually resistive and that it is unaffected by the variation of C_a. The third column shows how V_{ac} has been increased to maintain a constant amplitude of i_a across the increasing impedance of the equivalent load. The fourth column reveals that $|\Delta\theta_{La}|$ never exceeds 60° and that consequently, according to Fig. 9, the PIVT always operate in mode A. The fifth column highlights the phase adjusting property of the PIVT that successes in reducing $|\theta_{ia}|$ with respect to $|\Delta\theta_{La}|$.

Equation (30) has been used to obtain the nine blue lines plotted in the upper half of Fig. 16. Each of them corresponds to one value of V_{ac}/V_M given in Table II and to $\Delta\theta_{La}$ spanning the interval $(-60°, 0)$. As a matter of fact, Fig. 16 can be considered as a magnification of the upper-right part of Fig. 9. The blue circles are obtained inserting in (30) the $(V_{ac}/V_M, \Delta\theta_{La})$ pairs from Table II; each of them lies on a different line and represents the theoretical value of θ_{ia}. The red crosses, instead, correspond to the experimental value of θ_{ia}, reported on the fifth column of Table II.

Analysis of Fig. 16 shows that results from the experiments match very well with the expected ones and that PIVT is actually able to reduce the phase displacement between the currents when a reactive equivalent load is connected to the HFI outputs.

C. Efficiency Considerations

From the description given in Section III about the commutations of the power switches and of the diodes it derives that, with respect to the PST, the PIVT exhibits two additional zero-current commutations for each diode of LGa and LGb in each supply period. Other diode commutations happen at the turning ON and OFF of the power switches and are of the same type as those happening at the end of the dead times when the PST is used. Consequently, it can be concluded that the switching losses caused by the PIVT exceed those relevant to PST of the amount given by the zero-current commutation of the diodes. Moreover, in PIVT the diodes are flown by current for a comparatively long time so that their conduction losses should be considered whilst with the PST only the power switches are flown by current for most of the period.

The effect of the PIVT on the HFI efficiency have been explored by processing the samples of the input and output voltages and currents, acquired in the working conditions considered in Table II. The two last columns of the table report the average efficiency relevant to the PST and the PIVT. These quantities are plotted in the lower half of Fig. 16. Analysis of the data shows that at low values of $C_a/C_{a,N}$, the efficiency of PIVT is comparable with that of the PST whilst, for higher values of $C_a/C_{a,N}$, the PIVT performs a little worse. This behavior can be explained by supposing that the diodes switching losses do not affect much the overall efficiency of the HFI whilst it is more sensitive to the conduction losses of the diodes, which likely are higher than those of the power switches.

VII. Conclusion

This article proposes a modulation technique for a three-leg HFI that allows the simultaneous supply of two track coils of a WPTS. The amplitudes of the voltages supplying the two coils can be adjusted independently while maintaining the coil currents in phase for resistive HFI loads and reducing the current phase difference under the onset of a reactive component of the loads. The proposed technique has been deeply analyzed mathematically and then substantiated by experimental tests performed on a prototypal WPTS. The obtained results match very well with the expected ones. The efficiency measurement show that, adopting the proposed modulation technique, the losses of the HFI increases only marginally with respect to those of PST.

References

[1] S. Li and C. C. Mi, "Wireless power transfer for electric vehicle applications," *IEEE J. Emerg. Sel. Topics Power Electron.*, vol. 3, no. 1, pp. 4–17, Mar. 2015.

[2] V. Cirimele, M. Diana, F. Freschi, and M. Mitolo, "Inductive power transfer for automotive applications: State-of-the-art and future trends," *IEEE Trans. Ind. Appl.*, vol. 54, no. 5, pp. 4069–4079, Sep./Oct. 2018, doi: 10.1109/TIA.2018.2836098.

[3] R. Tavakoli and Z. Pantic, "Analysis, design, and demonstration of a 25-kW dynamic wireless charging system for roadway electric vehicles," *IEEE J. Emerg. Sel. Topics Power Electron.*, vol. 6, no. 3, pp. 1378–1393, Sep. 2018.

[4] H. K. Dashora, G. Buja, M. Bertoluzzo, R. Pinto, and V. Lopresto, "Analysis and design of DD coupler for dynamic wireless charging of electric vehicles," *J. Electromagn. Waves Appl.*, vol. 32, no. 2, pp. 170–189, 2018.

[5] G. Buja, M. Bertoluzzo, and H.K. Dashora, "Lumped track layout design for dynamic wireless charging of electric vehicles," *IEEE Trans. Ind. Electron.*, vol. 63, no. 10, pp. 6631–6640, Oct. 2016.

[6] C. Cheng, Z. Zhou, W. Li, C. Zhu, Z. Deng, and C. C. Mi, "A multi-load wireless power transfer system with series-parallel-series compensation," *IEEE Trans. Power Electron.*, vol. 34, no. 8, pp. 7126–7130, Aug. 2019, doi: 10.1109/TPEL.2019.2895598.

[7] Y. Wang, S. Zhao, H. Zhang, and F. Lu, "High-efficiency bilateral S–SP compensated multiload IPT system with constant-voltage outputs," *IEEE Trans. Ind. Inform.*, vol. 18, no. 2, pp. 901–910, Feb. 2022, doi: 10.1109/TII.2021.3072394.

[8] L. Shuguang, Y. Zhenxing, and L. Wenbin, "Electric vehicle dynamic wireless charging technology based on multi-parallel primary coils," in *Proc. IEEE Int. Conf. Electron. Commun. Eng.*, 2018, pp. 120–124.

[9] C. Wang, C. Zhu, K. Song, G. Wei, S. Dong, and R. G. Lu, "Primary-side control method in two-transmitter inductive wireless power transfer systems for dynamic wireless charging applications," in *Proc. IEEE PELS Workshop Emerg. Technol., Wireless Power Transfer*, 2017, pp. 1–6.

[10] J. Zhao, Y. Zhang, and L. Qi, "Design and analysis of a flexible multi-output wireless power transfer system with variable inductor," in *Proc. IEEE Energy Convers. Congr. Expo.*, 2021, pp. 1559–1564, doi: 10.1109/ECCE47101.2021.9595052.

[11] H. K. Dashora, M. Bertoluzzo, and G. Buja, "Reflexive properties for different pick-up circuit topologies in a distributed IPT track," in *Proc. IEEE Int. Conf. Ind. Inform.*, 2015, pp. 69–75.

[12] M. Bertoluzzo, G. Buja, and H. Dashora, "Avoiding null power point in DD coils," in *Proc. IEEE PELS Workshop Emerg. Technol., Wireless Power Transfer*, 2019, pp. 11–15.

[13] S. Huh and D. Ahn, "Two-transmitter wireless power transfer with optimal activation and current selection of transmitters," *IEEE Trans. Power Electron.*, vol. 33, no. 6, pp. 4957–4967, Jun. 2018, doi: 10.1109/TPEL.2017.2725281.

[14] D.-H. Kim and D. Ahn, "Maximum efficiency point tracking for multiple-transmitter wireless power transfer," *IEEE Trans. Power Electron.*, vol. 35, no. 11, pp. 11391–11400, Nov. 2020, doi: 10.1109/TPEL.2019.2919293.

[15] D.-H. Jang, "PWM methods for two-phase inverters," *IEEE Ind. Appl. Mag.*, vol. 13, no. 2, pp. 50–61, Mar./Apr. 2007.

[16] Y. Zhang et al., "Free positioning wireless charging system based on tilted long-track transmitting coil array," *IEEE Trans. Circuits Syst. II, Exp. Briefs*, vol. 69, no. 9, pp. 3849–3853, Sep. 2022, doi: 10.1109/TCSII.2022.3177617.

[17] SAE International, "Wireless power transfer for light-duty plug-in/electric vehicles and alignment methodology," Oct. 2020. Accessed: Jun. 6, 2022. [Online]. Available: https://saemobilus.sae.org/content/J2954_202010/

[18] C. Carretero, O. Lucía, J. Acero, and J. M. Burdío, "Phase-shift control of dual half-bridge inverter feeding coupled loads for induction heating purposes," *Electron. Lett.*, vol. 47, no. 11, pp. 670–671, May 2011.

[19] M. H. Rashid, *Power Electronics Circuits, Devices, and Applications*, 3rd ed. Englewood Cliffs, NJ, USA: Prentice-Hall, 2004.

[20] H. Dashora, M. Bertoluzzo, and G. Buja, "Dual-output inverter with phase correction ability for dynamic WPT track supply," in *Proc. 45th Annu. Conf. IEEE Ind. Electron. Soc.*, 2019, pp. 6349–6354, doi: 10.1109/IECON.2019.8927534.

[21] W. Zhang and C.C. Mi, "Compensation topologies of high-power wireless power transfer systems," *IEEE Trans. Veh. Technol.*, vol. 65, no. 6, pp. 4768–4778, Jun. 2016.

[22] U. Pratik, B. J. Varghese, A. Azad, and Z. Pantic, "Optimum design of decoupled concentric coils for operation in double-receiver wireless power transfer systems," *IEEE J. Emerg. Sel. Topics Power Electron.*, vol. 7, no. 3, pp. 1982–1998, Sep. 2019, doi: 10.1109/JESTPE.2018.2871150.

[23] R. Mai, Y. Luo, B. Yang, Y. Song, S. Liu, and Z. He, "Decoupling circuit for automated guided vehicles IPT charging systems with dual receivers," *IEEE Trans. Power Electron.*, vol. 35, no. 7, pp. 6652–6657, Jul. 2020, doi: 10.1109/TPEL.2019.2955970.

[24] G. Buja, M. Bertoluzzo, and K. N. Mude, "Design and experimentation of WPT charger for electric city car," *IEEE Trans. Ind. Electron.*, vol. 62, no. 12, pp. 7436–7447, Dec. 2015, doi: 10.1109/TIE.2015.2455524.

Manuele Bertoluzzo received the M.S. degree in electronic engineering and the Ph.D. degree in industrial electronics and computer science from the University of Padova, Padova, Italy, in 1993 and 1997, respectively.

Since 2015, he has been an Associate Professor with the Department of Electrical Engineering, University of Padova and holds the lectureship of road electric vehicles and systems for automation. He is involved in analysis and design of power electronics systems, especially for wireless charging of electric vehicles battery.

Giuseppe Buja (Life Fellow, IEEE) received the "Laurea" degree (with hons.) in power electronics engineering from the University of Padova, Padova, Italy, in 1970.

He is currently a Senior Research Scientist with the University of Padova. He has carried out an extensive research work in the field of power and industrial electronics, originating the modulating-wave distortion and the optimum modulation for pulsewidth modulation inverters. His current research interests include automotive electrification, including wireless charging of electric vehicles, and grid-integration of renewable energies.

Hemant Kumar Dashora (Member, IEEE) received the B.E. degree from the University of Rajasthan, Jaipur, India, in 2009, and the M.Tech. degree from the Indian Institute of Technology Kharagpur, Kharagpur, India, in 2011, both in electrical engineering.

He was a Senior Engineer with the General Motors Technical Centre, Bangalore, India, for almost 3 years. He focused on modeling and simulation of a complete architecture of hybrid and electric vehicles to analyze their fuel economy, performance, and durability. His current research interests include dynamic wireless charging of electric vehicles, coupling coil, and power supply analysis.